

## Impact of boron doping on electrical performance and efficiency of n-TOPCon solar cell

Qinqin Wang<sup>a,b</sup>, Wangping Wu<sup>c</sup>, Yunpeng Li<sup>a,b</sup>, Ling Yuan<sup>d</sup>, Sanchuan Yang<sup>d</sup>, Yufeng Sun<sup>d</sup>, Songbo Yang<sup>d</sup>, Qiang Zhang<sup>d</sup>, Yujia Cao<sup>d</sup>, Hui Qu<sup>d</sup>, Ningyi Yuan<sup>a,b,\*</sup>, Jianning Ding<sup>b,e,\*</sup>

<sup>a</sup> School of Materials Science and Engineering, Changzhou University, Changzhou 213164, PR China

<sup>b</sup> Jiangsu Collaborative Innovation Center of Photovoltaic Science and Engineering, Changzhou University, Changzhou 213164, PR China

<sup>c</sup> Electrochemistry and Corrosion Laboratory, School of Mechanical Engineering and Rail Transit, Changzhou University, Changzhou 213164, PR China

<sup>d</sup> Shunfeng Photovoltaic Technology, Changzhou 213164, PR China

<sup>e</sup> Institute of Intelligent Flexible Mechatronics, Jiangsu University, Zhenjiang 212013, PR China



### ARTICLE INFO

#### Keywords:

TOPCon solar cell  
B-doped profiles  
Peak concentration  
Junction depth  
B-selective emitters

### ABSTRACT

A big challenge to improve the conversion efficiency of n-type solar cell is the recombination and electrical contacting of boron (B)-doped emitters in n-TOPCon solar cells. This work investigates the emitter dark saturation current density under the passivation layer ( $J_{0e}$ , passivated), the metallization-induced recombination current density under the metal contact ( $J_{0e, metal}$ ), and the  $I$ - $V$  parameters, including short-circuit current density ( $J_{sc}$ ), open circuit voltage ( $V_{oc}$ ), fill factor (FF) and efficiency ( $E_{ff}$ ) as functions of the peak concentration ( $N_{max}$ ) and junction depth of B-doped profile. We introduced the profile with the peak concentration of  $1\text{--}1.5 \times 10^{19}$  atoms/cm<sup>3</sup> and a junction depth of 0.75–1.0  $\mu\text{m}$  to improve the conversion efficiency of 23.4%. The results revealed that  $J_{sc}$ , implied  $V_{oc}$  ( $iV_{oc}$ ) and the contact resistance ( $\rho_c$ ) were negative correlated with the  $N_{max}$  and junction depth. However,  $J_{0e}$ , passivated had a positive correlation with the same. The results from  $\rho_c$ ,  $J_{0e}$  along with the  $I$ - $V$  showed the junction depth of emitter doping profiles need to exceed the corroded depth of Ag/Al paste to get a low  $\rho_c$ , meanwhile, a low  $J_{0e}$  should be ensured. The results suggested the B-selective emitters were developed with a low  $\rho_c$  and a low  $J_{0e}$ . After optimizing B-selective emitters and passivation processes, we obtained industry-grade TOPCon cells with  $E_{ff}$ ,  $V_{oc}$ ,  $J_{sc}$ , and FF as high as 23.7%, 709 mV, 40.8 mA/cm<sup>2</sup>, and 82%, respectively. This optimized B-doped and simplified B-selective emitters processes can be commercially applied in photovoltaics.

### 1. Introduction

Phosphorus (P)-doped electron-selective contact (n-TOPCon) (Feldmann et al., 2013, 2014) solar cells are being studied extensively and large-scale commercialization of this technology appears promising. n<sup>+</sup>-poly-Si is fabricated through the following process (Polzin et al., 2018): (i) Growth of an interfacial oxide layer; (ii) Deposition of a doped amorphous Si layer (or a-Si layer); (iii) Recrystallization of the doped a-Si layer. Previous studies have reported the emitter recombination current of n<sup>+</sup>-poly-Si had a low density of approximately  $\sim 1.4 \text{ fA/cm}^2$  under the passivation layer ( $J_{0e}$ , passivated) on the polished surface (Tetzlaff et al., 2017), and its metallization-induced recombination current densities ( $J_{0e, metal}$ ) under the rear-contact was very low  $\sim 35 \text{ fA/cm}^2$

(Padhamnath et al., 2019), respectively. Meanwhile, high efficiencies of more than 26% were achieved via a tunnel-oxide passivation contact on an area of 4 cm<sup>2</sup> for n- and p-type substrates with either “front- and back-contacted” or “interdigitated back contact” architectures (Richter et al., 2018, 2020; Haase et al., 2018). Recently, for the front-side heavily B-doped p+ layer, B-doping recombination lower than  $11 \text{ fA/cm}^2$  @ 150 O/sqr has been reported on n-PERT solar cell (Ajay et al., 2020), however, its saturation current density at the Ag-Al contact increased to several 1,000 fA/cm<sup>2</sup> before optimization (Kiefer et al., 2014; Heinz et al., 2014; Lohmüller et al., 2014b; Edler et al., 2015; Wöhrl et al., 2016). And now, Lin et al. reported that its saturation current density can be  $<600 \text{ fA/cm}^2$  (Lin et al., 2020). Meanwhile, Zhu et al. showed that its saturation current density at the Al instead of Ag-Al contact decreased

\* Corresponding authors at: Jiangsu Collaborative Innovation Center of Photovoltaic Science and Engineering, Changzhou University, Changzhou 213164, PR China.

E-mail addresses: [nyyuan@cczu.edu.cn](mailto:nyyuan@cczu.edu.cn) (N. Yuan), [dingjn@cczu.edu.cn](mailto:dingjn@cczu.edu.cn) (J. Ding).

**Table 1**

Reviews on the research of B emitters for solar cell.

Emitter ( $p^+$ )	$R_{sheet}$ (ohm/sqr)	$N_{max}$ (atoms/cm <sup>3</sup> )	Junction ( $\mu m$ )	$J_{0e}$ (fA/cm <sup>2</sup> )	$J_{0e,met}$ (fA/cm <sup>2</sup> )	Cell parameters	Cell area	Structure	Important results	Ref.
Homogeneous emitter	140	$6 \times 10^{18}$	1.5	10	1800	$V_{oc}$ 703.6 mV, $J_{sc}$ 41.2 mA/cm <sup>2</sup> , FF 80.2%, $E_{ff}$ 23.2%.	Square: 20 mm $\times$ 20 mm	n-PERL	The negative-charge dielectric $Al_2O_3$ is an excellent front surface passivation layer on B-doped emitters	Benick et al., 2008.
Selective emitter	180	/	/	9	/	$V_{oc}$ 682.8 mV, $E_{ff}$ 21.04%	pseudo-square: 95 mm $\times$ 95 mm	n-TOPCon	The selective emitter resulting in $J_{sc}$ increase of 0.3 mA/cm <sup>2</sup> by wet chemical etch-back process	Tao et al., 2017
Selective emitter	200	/	/	6	397	$V_{oc}$ 670 mV, $E_{ff}$ 21%	pseudo-square: 95 mm $\times$ 95 mm	n- PERT	The selective emitter resulting in $J_{sc}$ increase of 0.4 mA/cm <sup>2</sup> and $E_{ff}$ 0.4% by APCVD	Upadhyaya et al., 2020
Homogeneous emitter	97	$5.0 \times 10^{19}$	/	45	1205	$V_{oc}$ 651 mV, $E_{ff}$ 20.31%	156 mm $\times$ 156 mm	n- PERT	The bulk lifetime of the wafers improved from 1.2 ms to 1.5 ms as a result of the co-diffusion process	Ryu et al., 2017
Homogeneous emitter	50	$3.4 \times 10^{19}$	0.6			Specific contact resistances well below 10 mohm.cm <sup>2</sup>	156 mm $\times$ 156 mm	$BBr_3$ -based B emitters with $AlO_x/SiN_x:H$ passivation layer on n-type c-Si	The addition of Te to the paste can change the temperature range where low specific contact resistances can be reached.	Fritz et al., 2016b
Homogeneous emitter	70			100		$V_{oc}$ 645.1 mV, $E_{ff}$ 20.1%	156 mm $\times$ 156 mm	n- PERT	A Boron emitter was developed using a $BCl_3$ doping process	Monna et al., 2016
Selective emitter	107	$4.3 \times 10^{19}$	0.45	25	740	/	156 mm $\times$ 156 mm	$BBr_3$ -based B emitters with $AlO_x/SiN_x:H$ passivation layer on n-type c-Si	The lower $N_{max}$ might result larger $J_{0,met}$ and higher specific contact resistance $\rho_c$ . Laser doping to form selective boron-doped emitters.	Lohmüller et al., 2018
Homogeneous emitter	614	$2 \times 10^{17}$	2	16.2	/	i $V_{oc}$ 688 mV, iFF 77.2%, $E_{ff}$ 15.9%	89 cm <sup>2</sup>	Epitaxially grown boron-doped Si emitters with $AlO_x/SiN_x:H$ passivation layer on n-type c-Si	A remote-plasma ALD $Al_2O_3$ /PECVD $SiN_x$ stack has a good passivation	Yoon et al., 2017
Homogeneous emitter	135	$1 \times 10^{19}$	0.95	14	/	i $V_{oc}$ 705 mV	156 mm $\times$ 156 mm	n- PERT	This new passivation method using the insitu grown $SiO_2$ during a $BBr_3$ diffusion process	Mihaletechi et al., 2018
Homogeneous emitter	90	/	0.5		348	$V_{oc}$ 655 mV, $E_{ff}$ 21.34%	156 mm $\times$ 156 mm	n- PERT	Using Al instead of Ag-Al can get higher $V_{oc}$ and lower $\rho_c$	Zhu et al., 2021
Homogeneous emitter	80	/	2	16	/	i $V_{oc}$ 700 mV	/	Using $BBr_3$ as the liquid boron source, resulting in a symmetrical p + np + structure.	The level of surface passivation change significantly with varying thickness of the $AlO_x$ capping layer	Dutta Gupta et al., 2012
Homogeneous emitter	92	$3 \times 10^{19}$	/	42	606	$V_{oc}$ 666 mV, $E_{ff}$ 20.7%	156 mm $\times$ 156 mm	n- PERT	An mechanism for enhanced recombination exists below the Ag/Al paste, which is especially detrimental for lowly doped emitters.	Kiefer et al., 2014
Selective TOPCon	120	/	/	8	430	$V_{oc}$ 707.5 mV, $E_{ff}$ 23.21%	158.75 mm $\times$ 158.75 mm	Selective n-TOPCon	The optimized design of the front surface TOPCon layer on the metal contact	Yu et al., 2021
Homogeneous emitter	200	$3 \times 10^{19}$	0.25	13	/	i $V_{oc}$ 700 mV, iFF 84.7%	/	n-TOPCon	The boron emitter diffusion was formed by rapid vapour phase direct doping (B-RVD)	Driene et al., 2020
Homogeneous emitter	90	/	/	/	446	/	/	$BBr_3$ -based B emitters with $AlO_x/SiN_x:H$	The deeper junctions effectively minimize the metal	Li et al., 2018

(continued on next page)

Table 1 (continued)

Emitter ( $p^+$ )	$R_{sheet}$ (ohm/sqr)	$N_{max}$ (atoms/cm <sup>3</sup> )	Junction ( $\mu m$ )	$J_{0e}$ (fA/cm <sup>2</sup> )	$J_{0e, metal}$ (fA/cm <sup>2</sup> )	Cell parameters	Cell area	Structure	Important results	Ref.
Homogeneous emitter	90	/	/	/	/	$V_{oc}$ 683.4 mV, $E_{ff}$ 22.14%	156 mm × 156 mm	passivation layer on n-type c-Si n-TOPCon	recombination at the metal–silicon interface. The sheet resistance and BSG thickness are affected by the $O_2$ flows.	Zhou et al., 2020
Homogeneous emitter	90	/	/	40	466.3	$V_{oc}$ 663 mV, $E_{ff}$ 20.9%	156 mm × 156 mm	n- PERT	The drive-in and the oxidation temperature are the most sensitive parameters with respect to solar cell efficiency	Li et al., 2019
Homogeneous emitter	66	$8.3 \times 10^{19}$	0.58	67	/	/	156 mm × 156 mm	n- PERT	1 The doping profiles feature 2 dopant concentrations of less than $8 \times 10^{19} \text{ cm}^{-3}$ , only thermionic emission and thermionic field emission have to be considered as current transport mechanisms ; 3 The deeper the junction, the lower $\rho_c$ . 3 the depletion zone itself is negligible with respect to $\rho_c$ .	Lohmüller et al., 2015
Homogeneous emitter	180	$5 \times 10^{18}$	1.4	12	706	$V_{oc}$ 702 mV, $E_{ff}$ 22.6%	239 cm <sup>2</sup>	n-TOPCon	Boron-doped surface contaminant limited the efficiency	Huang et al., 2020

to 348 fA/cm<sup>2</sup> (Zhu et al., 2021). But, the B-doped recombination is high enough compared with n<sup>+</sup>-poly-Si recombination. Therefore, the losses of n<sup>+</sup>-poly-Si recombination could be negligible in n-TOPCon solar cells.

Meanwhile, for mass-produced Si solar cells with industrial tunnel-oxide passivated contacts (i-TOPCon), lots of the largest PV manufacturers including CanadianSolar, GCL, JinkoSolar, Jolywood, SunPower, TrinaSolar, and Yingli have publicly reported the research on i-TOPCon (Hermle et al., 2020; Schultz-Wittmann et al., 2016; PV-magazine, 2020; Chen et al., 2019, 2020). Especially, the pilot lines efficiencies of JinkoSolar and TrinaSolar were reported above 24.5% (PV-magazine, 2020; Chen et al., 2020). Therefore, a big challenge about the further improvement of the conversion efficiency is the recombination and electrical contacting of B-doped emitters in n-TOPCon solar cells.

The preparation processes of B-doped emitter include BBr<sub>3</sub> tube diffusion (Padhamnath et al., 2019; Pal et al., 2019), B diffusion using boric acid (Ebrahimi et al., 2017), or B-ion implantation (Ok et al., 2016) and so on. However, the same requirements for B-doped emitters are to obtain a low emitter dark saturation current density ( $J_{0e}$ , passivated), resulting in obtaining a high open-circuit voltage ( $V_{oc}$ ). For achieving this, the front-side heavily B-doped p<sup>+</sup> layer should be lightly doped with a low peak concentration and a shallow junction. Meanwhile, a low specific contact resistance ( $\rho_c$ ) must be ensured for screen-printed metallization along with the high surface concentration of B-doped p<sup>+</sup> layer (Lohmüller et al., 2015; Werner et al., 2016). However, for achieving a low specific contact resistance of a few mΩ·cm<sup>2</sup> with screen-printed technology, a small amount of Al must be added to the Ag paste (Kopecek et al., 2005; Lago et al., 2010; Kerp et al., 2006). However, the screen-printed Ag/Al pastes initiate a stronger saturation current density at the metal contact, leading to severe losses of open-circuit voltage (Kiefer et al., 2014; Heinz et al., 2014; Edler et al., 2014; Wöhrle et al., 2016; Fritz et al., 2015; Koduvelikulathu et al., 2015; Kiefer et al., 2016; Li et al., 2018) due to the large metal crystallites formed at the interface between the Ag–Al bulk contact and the surface of the Ag–Al contacts (Heinz et al., 2014; Lohmüller et al., 2014a, 2014b; Edler et al., 2014; Wöhrle et al., 2016; Kopecek et al., 2005; Lago et al., 2010; Fritz et al., 2016a). This ultimately results in the loss of conversion efficiency. A

deep junction doping profile will be required to reduce the metallization-induced recombination losses (Li et al., 2019). Therefore, another major challenge to improve the efficiency is to achieve a high surface doping concentration with a low contact resistance to screen-printed Ag/Al metallization while maintaining highly homogenous emitter sheet resistance to minimize the emitter saturation current density (Schiele et al., 2014).

Here, we further summarize and briefly review the study of B emitters for solar cells (See Table 1). After reviewing the previous publications, the effect of B-doped profiles on the n-TOPCon solar cells, especially I–V parameters, has not yet been understood to a significant level. Therefore, this study focuses on the front-side B-doped profiles of n-TOPCon solar cells, which consists of screen-printed metallic contacts on both sides fabricated from 158.75 mm × 158.75 mm × 0.17 mm Cz–Si wafers through an industrial-type process with the fixed Ag–Al/Ag pastes. To this end, the peak concentration/junction depth of the B-doped profile was experimentally investigated with respect to their influences on  $J_{0e}$ , passivated,  $\rho_c$ ,  $J_{0e, metal}$ , and the I–V parameters of solar cells, i.e., efficiency ( $E_{ff}$ ), open-circuit voltage ( $V_{oc}$ ), fill factor (FF), series resistance ( $R_{ser}$ ) and short-circuit current density ( $J_{sc}$ ).

## 2. Experimental methods

### 2.1. Solar cell fabrication

We fabricated five types of samples: (a) the measurement of electrochemical capacitance voltage (ECV) sample with a symmetric double-sided B-doped layer on 0.8–1 Ω·cm n-type Cz–Si wafers; (b) the p<sup>+</sup>np<sup>+</sup> sample with a symmetric double-sided B-diffused and passivation with ALD–AlO<sub>x</sub>/PECVD SiN<sub>x</sub> stacks in order to extract the passivation layer ( $J_{0e}$ , passivated) on 5 Ω·cm n-type Cz–Si wafers; (c) the metallization-induced recombination ( $J_{0e, metal}$ ) sample with metal contacts printed on one side of the p<sup>+</sup>np<sup>+</sup> sample on 5 Ω·cm n-type Cz–Si wafers; (d) the measurement of specific contact resistance ( $\rho_c$ ) sample with H patterns (9 busbar – 110 fingers) on one side of the p<sup>+</sup>np<sup>+</sup> sample on 0.8–1 Ω·cm n-type Cz–Si wafers; (e) the structure of n-TOPCon cells (Fig. 1).

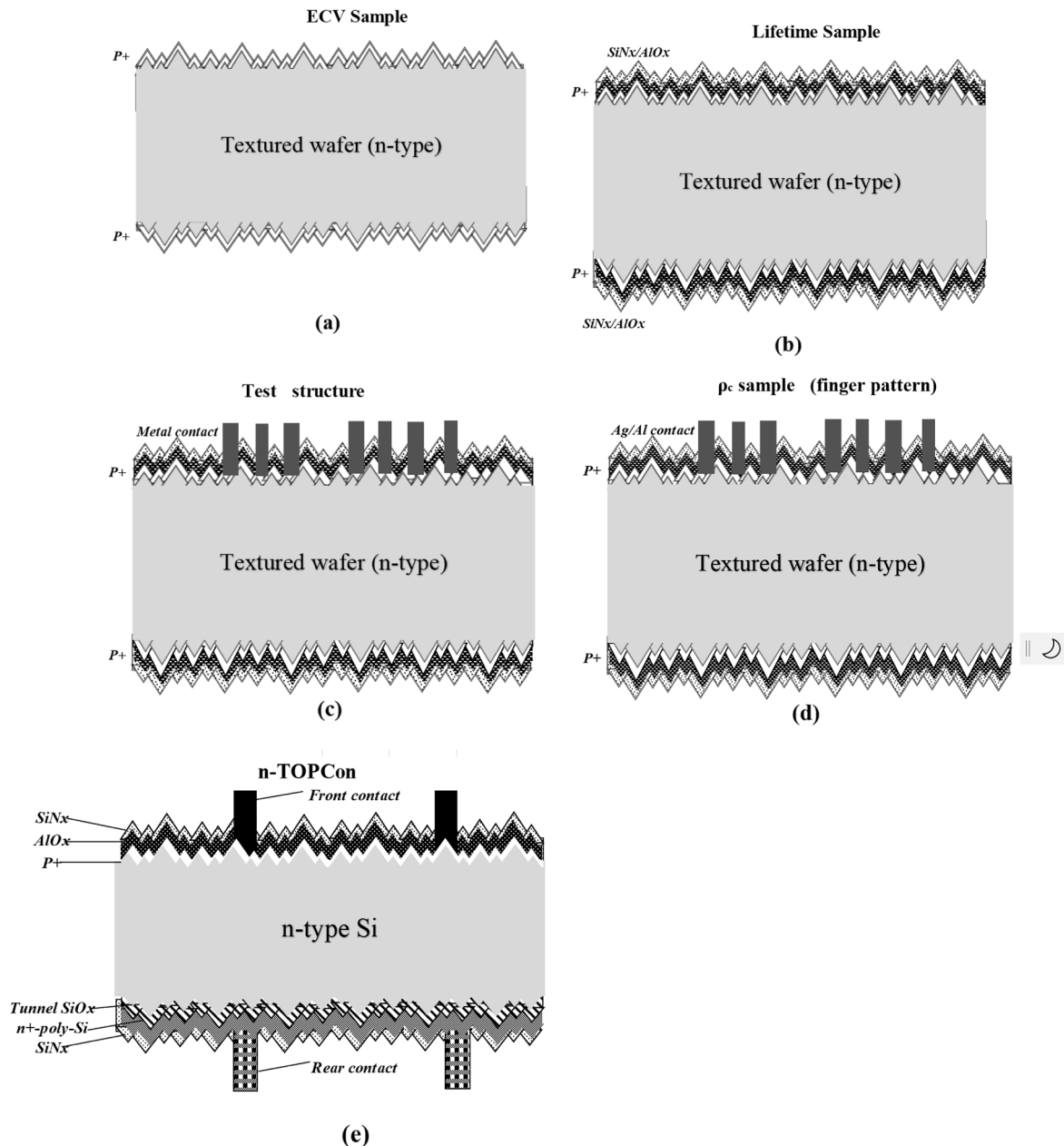


**Fig. 1.** Schematic illustration of (a) the measurement of electrochemical capacitance voltage (ECV) sample with a symmetric double-sided B-doped layer on 0.8–1  $\Omega\text{-cm}$  n-type Cz-Si wafers; (b) the  $p^+np^+$  sample with a symmetric double-sided B-diffused and passivation with ALD- $\text{AlO}_x$ /PECVD  $\text{SiN}_x$  stacks in order to extract the passivation layer ( $J_{0e}$ , passivated) on 5  $\Omega\text{-cm}$  n-type Cz-Si wafers; (c) the metallization-induced recombination ( $J_{0e}$ , metal) sample with metal contacts printed on one side of the  $p^+np^+$  sample on 5  $\Omega\text{-cm}$  n-type Cz-Si wafers; (d) the measurement of specific contact resistance ( $\rho_c$ ) sample with H patterns (9 busbar–110 fingers) on one side of the  $p^+np^+$  sample on 0.8–1  $\Omega\text{-cm}$  n-type Cz-Si wafers; (e) a P-doped electron-selective contact (n-TOPCon) solar cell with B-diffused  $p^+$  layer at the front side.

We manufactured the n-TOPCon cells from commercially available 158.75 mm  $\times$  158.75 mm n-type Cz-Si wafers with 0.8–1  $\Omega\text{-cm}$  electrical resistivity. The Si wafer thickness was  $160 \pm 10 \mu\text{m}$ . The cell fabrication sequence has been introduced in a previous work (Wang et al., 2020a, 2020b). All wafers were textured in alkaline (KOH) solution and subsequently cleaned in a mixture solution of HCl and HF. The front B emitter was formed in a quartz tube furnace containing  $\text{BCl}_3$  gas using LYDOP™ system technology (SEMCO) (Oliver et al., 2010; Armand et al., 2011).

The ECV samples on 0.8–1  $\Omega\text{-cm}$  n-type Cz-Si wafers were obtained by HF (15%) cleaning the diffused sample to remove the borosilicate glass (BSG) layer (Peiner et al., 1995; Bock et al., 2008). The deposition time, drive-in, oxidation time and oxidation temperature of the  $\text{BCl}_3$

diffusion processes (See Table 2) were adapted such that the B-doped profiles featured nearly identical curve progressions up to a depth of  $d \approx 100 \text{ nm}$ . The depletion of the B concentration close to the surface results from the post-oxidation step performed at the end of the  $\text{BCl}_3$  diffusion processes, because the solubility of B is higher in silicon oxide than in silicon (Grove et al., 1964). Different junction depths are determined at a dopant concentration of  $N = 10^{16} \text{ atoms/cm}^3$ . In this study, we conducted two types of experiments, whose specifications are as shown in Table 1. In the first type, we varied the peak concentration under a constant junction depth: 1) emitter type D1 [ $d_1 \approx 0.5 \mu\text{m}$  ( $N_{\max} \approx 1.15 / 2.23 / 2.89 \times 10^{19} \text{ atoms/cm}^3$ )], 2) emitter type D2 [ $d_2 \approx 0.63 \mu\text{m}$  ( $N_{\max} = 1.22 / 1.49 / 4 \times 10^{19} \text{ atoms/cm}^3$ )], 3) emitter type D3 [ $d_3 \approx 0.8 \mu\text{m}$  ( $N_{\max} \approx 1.94 / 2.63 / 3.14 \times 10^{19} \text{ atoms/cm}^3$ )] (Fig. 2a/b/c). In the

**Table 2**The process parameters of  $\text{BCl}_3$  diffusion.

Emitters	$N_{\text{max}}$ (atoms/cm <sup>3</sup> )	Depth ( $\mu\text{m}$ )	Deposition (min)	Drive in (min)	Oxidation (min)	Oxidation T (°C)	$\text{BCl}_3$ (ml/min)
D1	1.15E + 19	0.5	5	0.5	70	950	10
	2.23E + 19			7	20		
	2.89E + 19			15	20		
D2	1.22E + 19	0.63	5	5	50	990	
	1.49E + 19			10	20		
	4.00E + 19			20	20		
D3	1.94E + 19	0.8	5	5	55	990	
	2.63E + 19			12	40		
	3.14E + 19			20	40		
N1	3.00E + 19	0.5	5	15	20	950	
				18	40		
				26	50		
N2	2.60E + 19	0.5	3	8	20	950	
			0.85	12	40		

second type, the junction depth was varied under the same peak concentration: 1) emitter type N1 [ $N_1 \approx 3 \times 10^{19}$  atoms/cm<sup>3</sup> (0.5/0.8/1.0  $\mu\text{m}$ )] and 2) emitter type N2 [ $N_2 \approx 2.6 \times 10^{19}$  atoms/cm<sup>3</sup> (0.5/0.85  $\mu\text{m}$ )] (Fig. 2d/e).

ALD- $\text{AlO}_x$ /PECVD- $\text{SiN}_x$  stacks were deposited on both sides of the  $\text{p}^+\text{np}^+$  structure samples and the test structure samples on 5  $\Omega\cdot\text{cm}$  n-type Cz–Si wafers. While  $\text{AlO}_x$  had a thickness of 3 nm,  $\text{SiN}_x$  had a thickness of 80 nm. The same types of samples with pyramid-textured surfaces as in the  $\text{p}^+\text{np}^+$  structure samples were screen-printed with Ag/Al contact lines only on one side, with four different pitches as the test structure. Then, the Ag/Al paste was exposed to fire in an industrial belt-firing furnace at a peak firing temperature of 750 °C with the finger-side facing up. Subsequently, the fingers were etched off with aqua regia ( $V_{\text{HCl}}:V_{\text{HNO}_3} = 3:1$ ). Finally, the samples were rinsed in deionized (DI) water and oven dried. The  $J_{0e}$  values for the four metallization fractions  $f$  were calculated using the same Sinton WCT-120 tool as for the earlier  $J_{0e}$  measurements. Meantime, the specific contact resistance ( $\rho_c$ ) sample was achieved from printed H patterns (9 busbar –110 fingers) on one side of the  $\text{p}^+\text{np}^+$  sample on 0.8–1  $\Omega\cdot\text{cm}$  n-type Cz–Si wafers.

The rear side after B diffusion was etched using a mixed solution of HF/HNO<sub>3</sub>. The rear side of the  $\text{SiO}_x$  (1.2–2 nm) / a-Si (150 ± 20 nm) layers were deposited by low-pressure chemical vapor deposition (LPCVD). Subsequently, the as-prepared samples were annealed in a tube furnace at 900 °C for 45 min in a mix of  $\text{POCl}_3$ , O<sub>2</sub>, and N<sub>2</sub> to crystallize the a-Si to poly-Si. In the next cleaning BSG/ phosphorsilicate glass (PSG) removal step, the poly-Si wraparound side was etched in inline treatment with HF/HNO<sub>3</sub> and batch-type treatment with KOH/ polish additives solution, to have only one side with n<sup>+</sup>-poly-Si layer (Wang et al., 2020b). Then, the front and rear passivation of the cell was fabricated by 3 nm- $\text{AlO}_x$ /80 nm- $\text{SiN}_x$  and 80 nm- $\text{SiN}_x$ , respectively. The wafer was metallized by screen-printed and firing of a metal paste using an H-patterned grid design on both sides. A commercial Ag/Al paste and Ag paste were used for the front-side metal grid and the rear, respectively. The 9-busbar (BB) configuration was used for both the front and rear sides. Then, the cells were manufactured by fast firing the wafer in a conveyor belt furnace at a peak firing temperature of 750 °C.

## 2.2. Characterization

The current–voltage ( $I$ – $V$ ) parameters were measured using a DENKEN tester after calibration by a Fraunhofer ISE standard cell. The implied  $V_{\text{oc}}$  ( $iV_{\text{oc}}$ ) values of the controlled samples were determined by a lifetime tester under 1-sun illumination (WCT-120 Sinton, Boulder, CO, USA). The  $J_{0e}$ , passivated and  $J_{0e,\text{metal}}$  values of the samples were measured by WCT-120 Sinton and extracted at the excess carrier density of  $3 \times 10^{15}$  cm<sup>−3</sup> (Liu et al., 2016) (Boulder, CO, USA). The B-doped profiles of monitor wafers were measured by ECV device (WEP CVP21) using a 0.1 M NH<sub>4</sub>F solution as the etchant. The microstructure and morphology of

the previously metallized areas after removing the metal paste, the glass layer, and the dielectric passivation layer stack by a wet-chemical etching process were measured by scanning electronic microscopy (SEM, Quanta FEG 250, FEI). The specific contact resistance ( $\rho_c$ ) of the screen-printed metallized contact with different profiles was determined by the transfer-length-method (TLM) (GP-4 TEST). The optical reflectance of the cell was measured by PVE300-IVT. During these tests, the optical losses were analyzed by Current Loss Analysis Calculator V1.4 (the Solar Energy Research Institute of Singapore) (Wong et al., 2016).

## 3. Results and discussion

### 3.1. Emitter dark saturation current density of the B-diffused/ $\text{AlO}_x/\text{SiN}_x$ structure

It is important to estimate the surface passivation performance of the B-doped front surface of the cells because the passivated region occupies greater than 95% front surface. Therefore, effective passivation of the B-doped surface is integral to design high-efficiency n-TOPCon solar cell. More importantly, it is essential to understand the change in the passivation quality with the B-doped profile. In this subsection, we explain that in order to evaluate the emitter passivation quality in the passivated  $\text{p}^+$  layers, the symmetrical samples were B-diffused and passivated by  $\text{AlO}_x/\text{SiN}_x$  films (Fig. 1b). The values of  $J_{0e}$ , passivated with different peak concentrations and junction depths were determined from quasi-steady-state photoconductance measurements and Kane and Swanson's proposal (Kane and Swanson, 1985) on testing 3–4 wafers at 3 points per piece (Fig. 3). In the case of emitter D1,  $J_{0e}$ , passivated can be increased from 18.4 to 22.3 fA/cm<sup>2</sup> by increasing the peak concentration from 1.15 to  $2.89 \times 10^{19}$  atoms/cm<sup>3</sup> at  $d_1 = 0.5 \mu\text{m}$  (Fig. 3a). A low surface dopant concentration leads to a low interface state density, which further leads to a low surface recombination velocity (Altermatt et al., 2002). The same trend can be observed for emitters D2 ( $d_2 = 0.63 \mu\text{m}$ ) and D3 ( $d_3 = 0.8 \mu\text{m}$ ) (Fig. 3b&c). For the emitter D2,  $J_{0e}$ , passivated increased from 15.7 to 44.4 fA/cm<sup>2</sup> by increasing the peak concentration from 1.22 to  $4 \times 10^{19}$  atoms/cm<sup>3</sup> at  $d_1 = 0.63 \mu\text{m}$  (Fig. 3b). For the emitter D3,  $J_{0e}$ , passivated increased from 23.3 to 39.9 fA/cm<sup>2</sup> by increasing the peak concentration from 1.94 to  $3.14 \times 10^{19}$  atoms/cm<sup>3</sup> at  $d_1 = 0.8 \mu\text{m}$  (Fig. 3c). However, we found that the peak concentration on the deep junctions (emitters D2 & D3) has a stronger impact on the value of  $J_{0e}$ , passivated than that on the shallow junction (emitters D1). Perhaps because the deep junctions have high bulk recombination, and then they are sensitive to surface concentration. As shown in Fig. 3c, the value of  $J_{0e}$ , passivated increased from 22.3 to 42.8 fA/cm<sup>2</sup> with the increase in the junction depth from 0.5 to 1.0  $\mu\text{m}$  on the peak concentration of  $3 \times 10^{19}$  atoms/cm<sup>3</sup>. And in Fig. 3d,  $J_{0e}$ , passivated increased from 22.4 to 36.4 fA/cm<sup>2</sup> by increasing the junction depth from 0.5 to 0.85  $\mu\text{m}$  at the peak concentration of  $2.6 \times 10^{19}$  atoms/cm<sup>3</sup>. In Fig. 3f, as

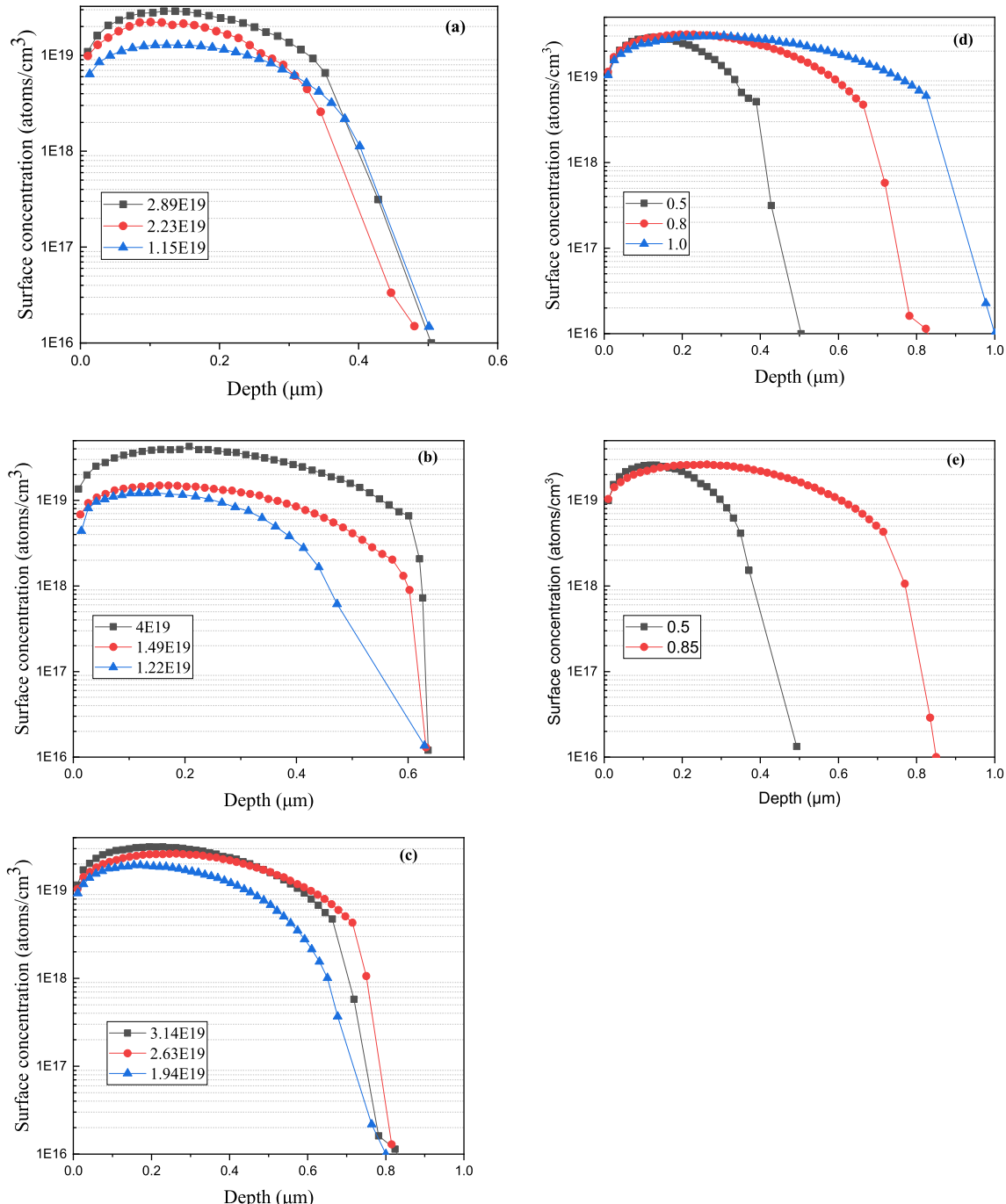


**Fig. 2.** ECV profiles of the change in the peak concentrations under one constant junction depth (a) Emitter D1 ( $d_1 \approx 0.5 \mu\text{m}$ ), (b) Emitter D2 ( $d_2 \approx 0.63 \mu\text{m}$ ), (c) Emitter D3 ( $d_3 \approx 0.8 \mu\text{m}$ ); the change in junction depths under one constant peak concentration (d) Emitter N1 ( $N_1 \approx 3 \times 10^{19} \text{ atoms/cm}^3$ ) and (e) Emitter N2 ( $N_2 \approx 2.6 \times 10^{19} \text{ atoms/cm}^3$ ).

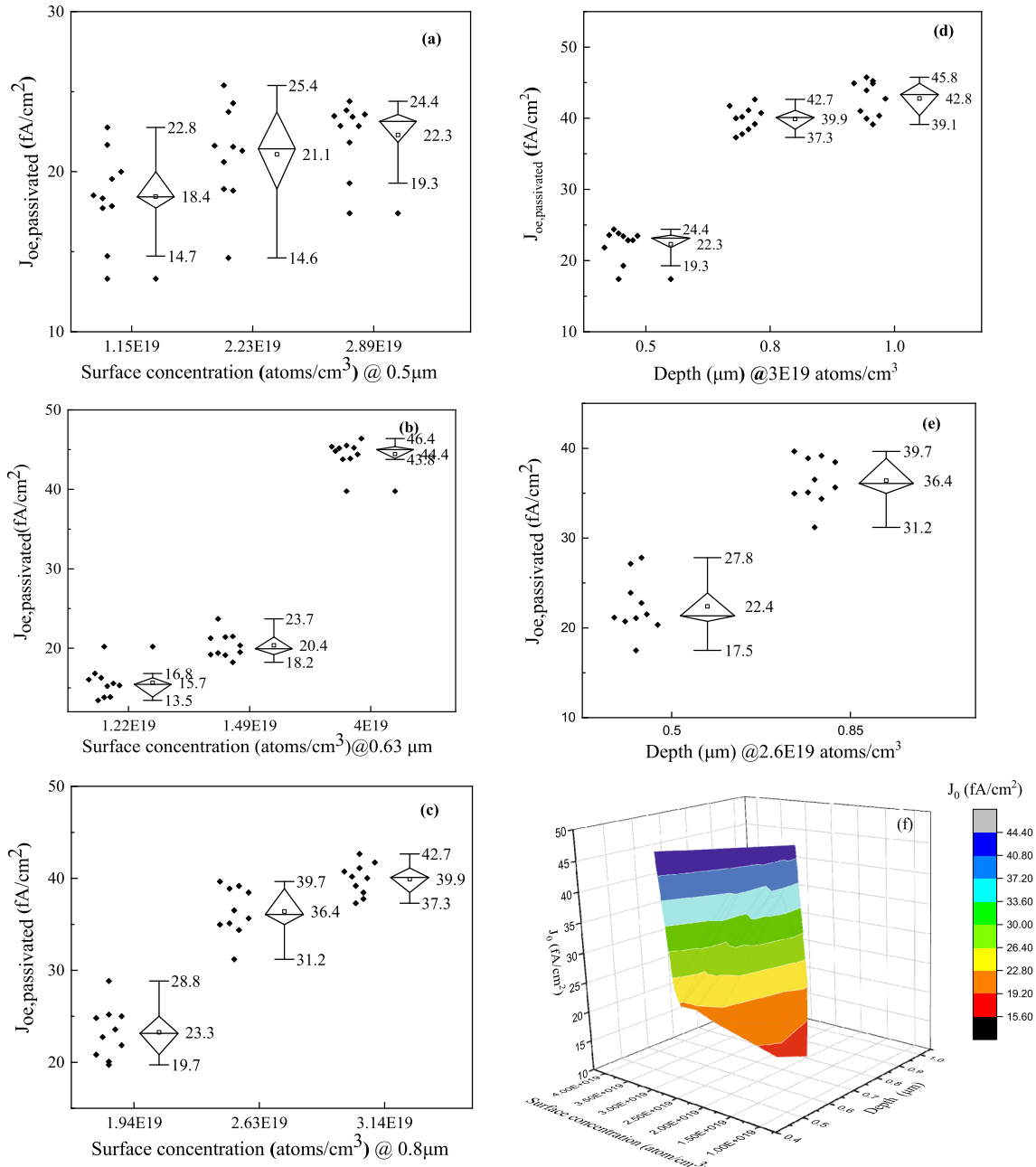


**Fig. 3.** Emitter dark saturation current densities in the passivated regions of (a) emitter D1, (b) emitter D2, (c) emitter D3, (d) emitter N1 and (e) emitter N2. And (f) the  $J_{oe, \text{passivated}}$  as a function of the junction depth and the peak concentration of B-doped profile.

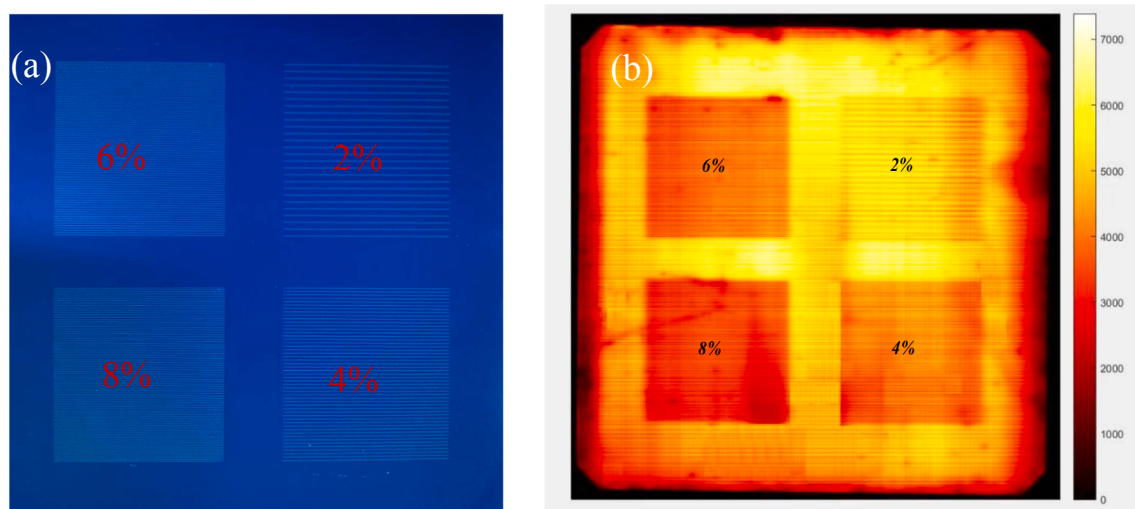


**Fig. 4.** The photograph of the screen-printing pattern of the sample with different metallization fraction from 2% to 8% (a) and Photoluminescence (PL) image (b) of the symmetrical samples were boron-diffused and passivated by  $\text{Al}_2\text{O}_3/\text{SiN}_x$  films with four different metallization fractions on the front side. The metal was etched away before the PL measurement. The numbers in percentage indicate the metallization fractions.

the junction depth and the peak concentration increased, the value of  $J_{0e}$ , passivated changed in the same direction because of the large surface and bulk recombination, which has a higher doping density due to lowered minority mobility. To reduce  $J_{0e}$ , passivated, the B-doped profiles should have a low dopant concentration and a shallow junction.

A firing-through Ag/Al paste was used to metallize the passivated  $\text{p}^+$  layers. Because the paste may deteriorate the passivation ability of the stack, the samples with four different metallization fractions were screen-printed, as described in Subsection 2.1. Fig. 4a illustrates the photograph of screen-printing pattern of the sample with different metallization fractions and Fig. 4b shows the photoluminescence (PL) image of a sample after firing and removing the Ag/Al contact lines. References (Fellmeth et al., 2011, Chen et al., 2020) presented the formula of  $J_{0e}$ , metal based on a simple linear interpolation of the measured data points (Fig. S1). In this study,  $J_{0e}$ , metal was extracted from the Sinton tests of the samples (three pieces of solar cells were fabricated for metal coverage per boron profile) (Fig. S2). Profiles with a higher peak concentration on a constant junction depth(D1/D2/D3) (Fig. 5a-c) exhibit a significantly lower  $J_{0e}$ , metal, i.e., it decreases from  $828 \text{ fA/cm}^2$  ( $1.15 \times 10^{19} \text{ atoms/cm}^3$ ) to  $645 \text{ fA/cm}^2$  ( $2.89 \times 10^{19} \text{ atoms/cm}^3$ ), and from  $711.2 \text{ fA/cm}^2$  ( $1.22 \times 10^{19} \text{ atoms/cm}^3$ ) to  $342.4 \text{ fA/cm}^2$  ( $4 \times 10^{19} \text{ atoms/cm}^3$ ), and from  $550 \text{ fA/cm}^2$  ( $1.94 \times 10^{19} \text{ atoms/cm}^3$ ) to  $412 \text{ fA/cm}^2$  ( $3.14 \times 10^{19} \text{ atoms/cm}^3$ ), respectively. These results can be explained by the “transport limited emitters” concept (del Alamo and Swanson, 1984), which are less sensitive to bulk recombination because the hole concentration in the most highly doped layers of the emitters, near the surface where the lifetime is very degraded and become short. Therefore, the hole recombination rate is small too. The effect of increasing the doping level is to reduce  $J_0$ . According to these results, the peak concentration had a more remarkable effect in shallow emitter D1/D2 than deep emitter D3 within the investigated range.

For the same peak concentration,  $J_{0e}$ , metal exhibits a simple linear interpolation with junction depth ( $<0.85 \mu\text{m}$ ), as shown in Fig. 5d&e. This relationship can be also explained by the “transport limited emitters” concept of del Alamo et al.’s theory (del Alamo and Swanson, 1984), which can increase the doping thickness and then reduce  $J_0$  value. However, the  $J_{0e}$ , metal of the sample with the deep junction of  $1.0 \mu\text{m}$  increases up to  $699.3 \text{ fA/cm}^2$  (Fig. 5d), possibly due to not only the penetration of the metal into the emitter region but also the increase in junction depth with the high bulk recombination. As illustrated in Fig. 5f, the measured  $J_{0e}$ , metal was analyzed by the junction depth and the peak concentration. Under fixed metallization conditions, the degree of the metallization-induced recombination losses was significantly

dependent on the doping profile. To obtain a good  $J_{0e}$ , metal, a higher peak concentration and appropriate junction is required, rather than the deepest junction.

### 3.2. Microstructure at metal–Si interface

Fig. 6a presents the typical top-view SEM micrograph of emitter D3 ( $1.94 \times 10^{19} \text{ atoms/cm}^3$ ) etched in aqua regia. The corroded pyramid structure was present on the surface of the cell, which had a width of more than  $1.2 \mu\text{m}$ . The Ag/Al paste does not uniformly corrode the B-doped layer. In Fig. 6b, the corroded depth is approximately  $0.45\text{--}0.63 \mu\text{m}$ —clearly 5 times larger than the depletion zone depth. The effect of the depletion zone on the  $\rho_c$  could be negligible (Lohmüller et al., 2015). In Fig. 6c, the width of the corrosion hole is approximately  $0.38 \mu\text{m}$  within the investigated range. According to Wöhrle et al. (Wöhrle et al., 2016), the heavy increase in  $J_{0e}$ , metal started until the tips reached depths where the B-doped concentration was lower than approximately  $10^{18} \text{ atoms/cm}^3$  for all profiles. Therefore, we inferred that  $J_{0e}$ , metal is not significantly affected at depths of greater than  $0.63 \mu\text{m}$  when a dopant concentration was equal to  $10^{18} \text{ atoms/cm}^3$ . This is because the effect of the peak concentration on  $J_{0e}$ , metal in shallow emitter D1 and D2 is more significant than that in deep emitter D3. The sample with the junction depth of  $1.0 \mu\text{m}$  had a higher  $J_{0e}$ , metal because the deeper emitter had a high bulk recombination (Edler et al., 2014).

### 3.3. Contact resistance

The specific contact resistance  $\rho_c$  for the tested structure with the sample is shown in Fig. 7. Lohmüller et al. (Lohmüller et al., 2015) reported that the macroscopically measured specific contact resistance  $\rho_c$  can be explained, assuming that current is transported exclusively via crystallites in direct contact with the Ag-Al contact bulk and the B-doped emitter when the dopant concentration is less than  $8 \times 10^{19} \text{ cm}^{-3}$ . The confidence interval for the median of the specific contact resistance values was illustrated by the notched box plot. In the case of varying emitters (D1–D3), the specific contact resistance can be decreased significantly from  $4.5$  to  $1.1 \text{ m}\Omega\cdot\text{cm}^2$  by increasing the peak concentration, as shown in Fig. 7a–c. Meantime, the specific contact resistance can be decreased significantly from  $3.1$  to  $1.1 \text{ m}\Omega\cdot\text{cm}^2$  by increasing the junction depth from  $0.5$  to  $0.85 \mu\text{m}$  for the same peak concentration (emitters N1&N2, Fig. 7d–e) and approached a flat after the junction depth reached  $1.0 \mu\text{m}$ . To analyze the influence of the process parameters on the specific contact resistance, the  $\rho_c$  values of the B-doped

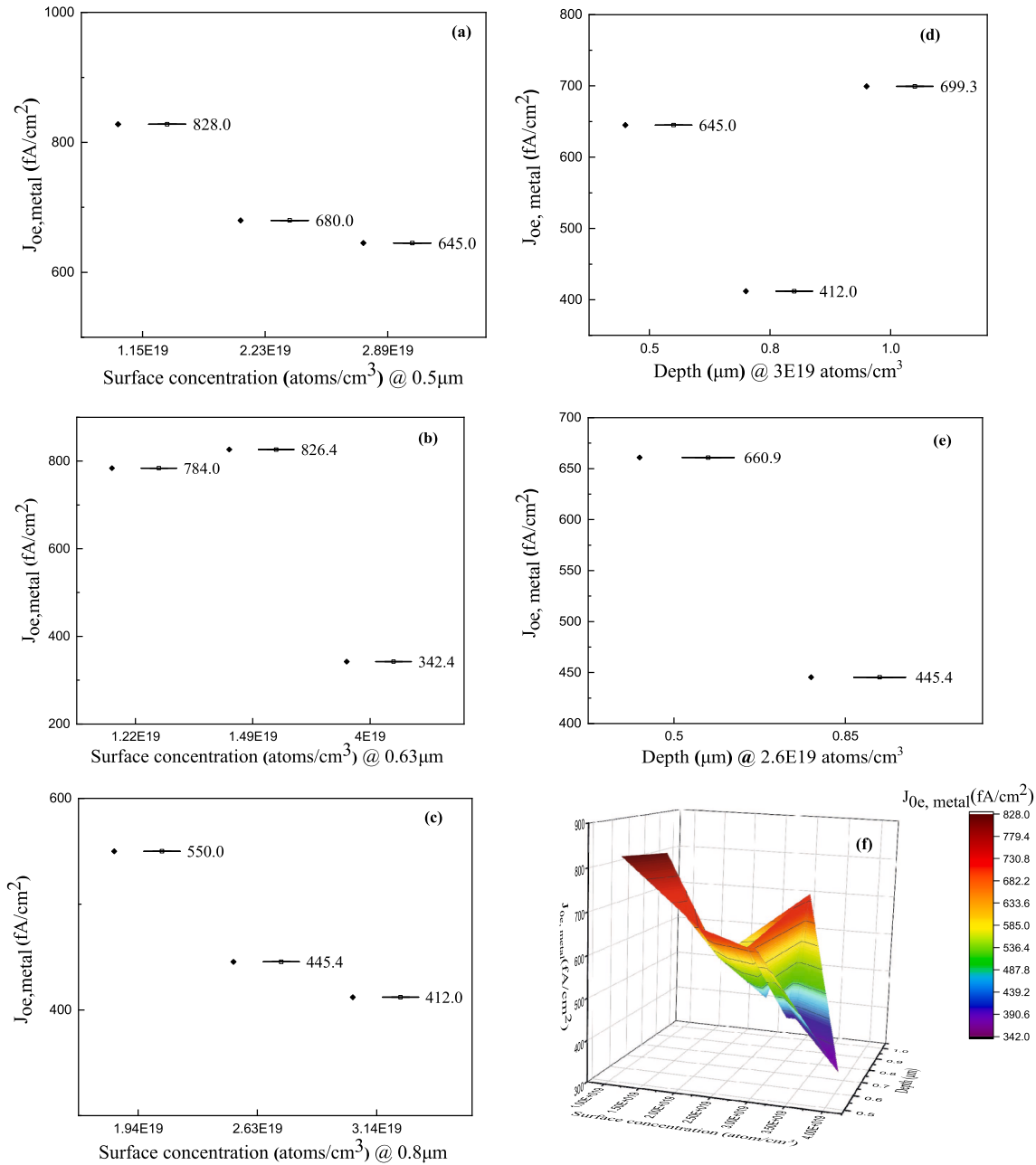


**Fig. 5.** The plots of emitter dark saturation current densities in the passivation on the contact regions of (a) emitter D1, (b) emitter D2, (c) emitter D3, (d) emitter N1, (e) emitter N2 and (f) the 3D-plot of  $J_{0e, \text{metal}}$  as a function of the junction depth and the peak concentration of B-doped profile.

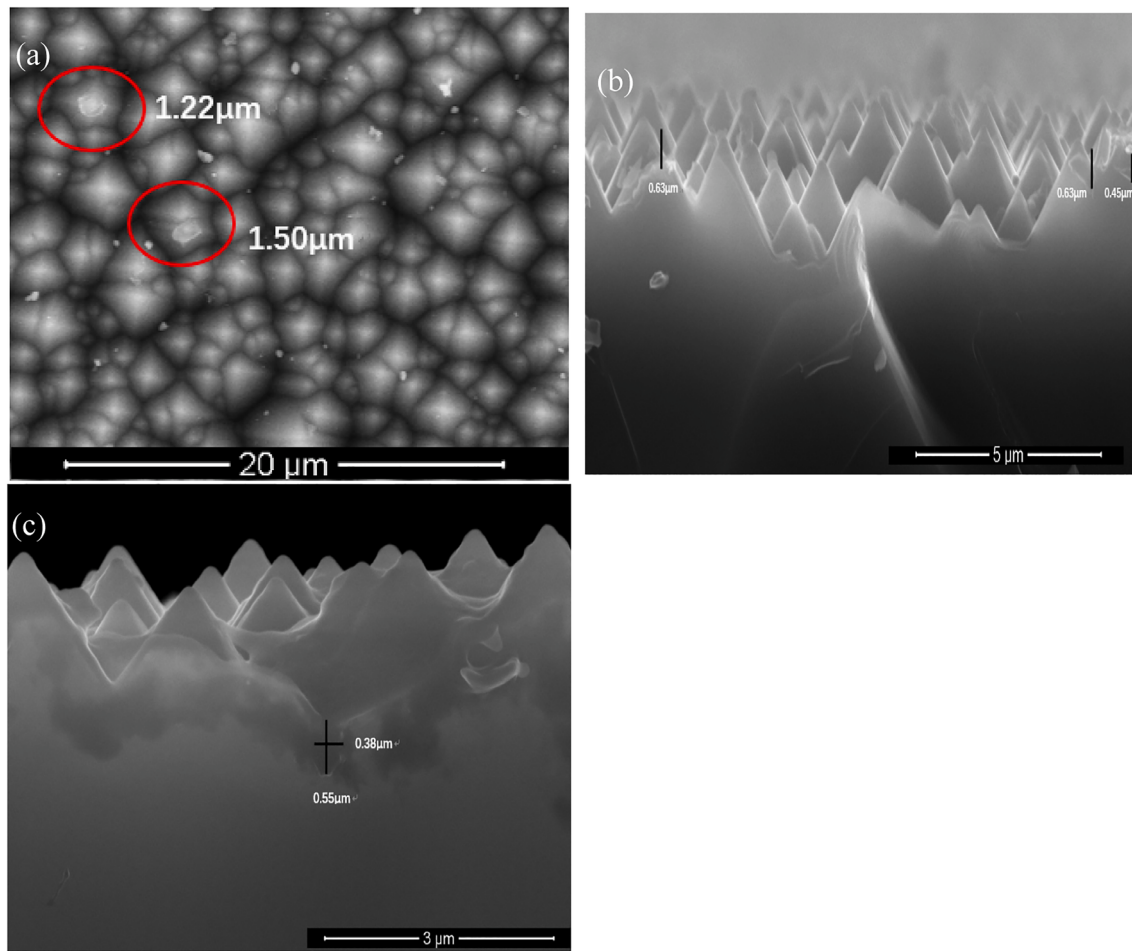


**Fig. 6.** (a) Scanning electron microscopy (SEM) image of emitter D3 sample ( $1.94 \times 10^{19}$  atoms/cm $^3$ ) surface after etching away the Ag–Al contact, the glass layer, the passivation layer, and all spikes. Remaining spikes imprints in red circles; (b)/(c) SEM cross section of contact spot. The shape of a corroded pyramid can be clearly seen.

profiles were estimated, according to a graphical linear interpolation in Fig. 7f. The figure reveals a linear relationship between  $\rho_c$  and the peak concentration/depth junction (Durán et al., 1991; Fritza et al., 2013). To obtain a suitable  $\rho_c$ , a high peak concentration and deep junction of B-doped profiles were required because a high dosage of B doping can improve the electrical conductivity.

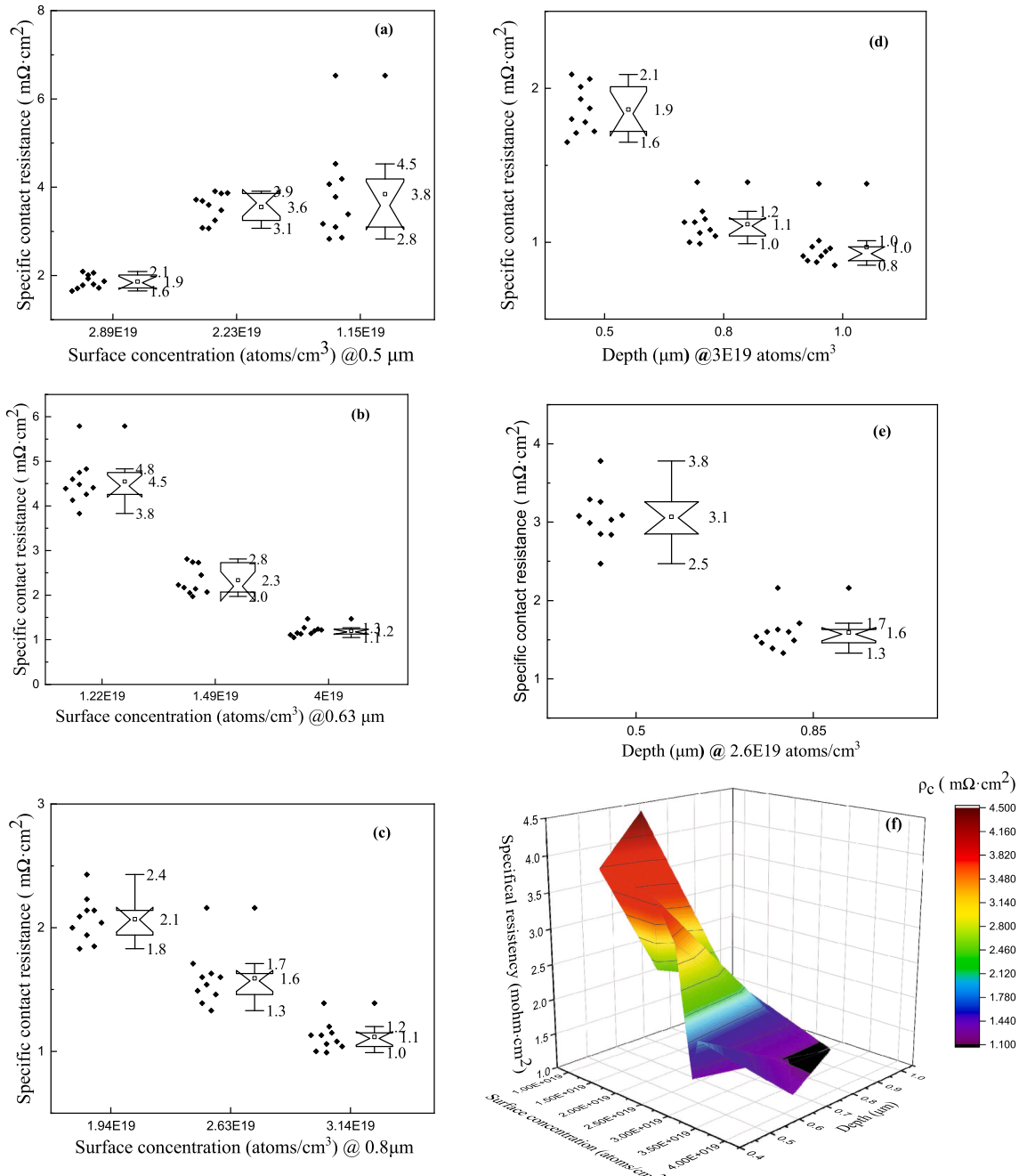
#### 3.4. Precursor $iV_{oc}$

Fig. 8 shows the  $iV_{oc}$  and effective lifetime of the precursor structure wafers without metallization measured by the quasi-steady-state photoconductance technique (QSSPC) (Sinton et al., 1996). The values on the effective lifetime curve indicate  $iV_{oc}$  at the excess carrier density of  $1 \times 10^{15}$  cm $^{-3}$  under 1-sun illumination. The profiles with a high peak concentration on a constant junction depth D1, D2, D3 (Fig. 8a-c) exhibited a significantly low  $iV_{oc}$ , i.e., it decreased from 721 (1.15  $\times 10^{19}$  atoms/cm $^3$ ) to 712 mV (2.89  $\times 10^{19}$  atoms/cm $^3$ ) on emitter D1, and from 717 (1.22  $\times 10^{19}$  atoms/cm $^3$ ) to 699 mV (4  $\times 10^{19}$  atoms/cm $^3$ ) on emitter D2, and from 712 (1.94  $\times 10^{19}$  atoms/cm $^3$ ) to 703 mV (3.14  $\times 10^{19}$  atoms/cm $^3$ ) on emitter D3, respectively. However, with increasing the peak concentration on the same junction depth (e.g.,

emitter D1 with  $1.15 - 2.23 \times 10^{19}$  atoms/cm $^3$ , emitter D2 with  $1.22 - 1.49 \times 10^{19}$  atoms/cm $^3$  and emitter D3 with  $2.63 - 3.14 \times 10^{19}$  atoms/cm $^3$ ), the difference in the  $iV_{oc}$  values is below 2 mV, which can be ignored. However, there is a distinct effective lifetime at the excess carrier density from  $1 \times 10^{14}$  to  $1.5 \times 10^{16}$  cm $^{-3}$ . And increasing the junction depth on the same peak concentration, a degradation  $iV_{oc}$  values as high as 27 mV is observed from 0.5 to 1.0  $\mu\text{m}$  (Fig. 8d). This trend is strong for the effective lifetime at the excess carrier density from  $1 \times 10^{14}$  to  $1.5 \times 10^{16}$  cm $^{-3}$  (Fig. 8d and e). These results indicate that the junction depth has a stronger influence on the  $iV_{oc}$  and effective lifetime than the peak concentration. To obtain a suitable  $iV_{oc}$  and effective lifetime, an appropriate peak concentration and shallow junction of B-doped profiles are required.

#### 3.5. I-V parameters

Table 3 illustrates the I-V parameters of the cells at 4–5 pieces of solar cells per boron profile. And the box plots are shown in Fig. S3 and Fig. S4. The D3 sample with the peak concentration =  $1.94 \times 10^{19}$  atoms/cm $^3$  exhibited the best electrical performance, having a high  $E_{ff}$  (23.34%), high  $V_{oc}$  (702 mV), and high  $J_{sc}$  (41.01 mA/cm $^2$ ), rather than



**Fig. 7.** Specific contact resistance (tested by TLM) for (a) emitter D1, (b) emitter D2, (c) emitter D3, (d) emitter N1 and (e) emitter N2. And (f) the Specific contact resistance as a function of the junction depth and the peak concentration of B-doped profile.

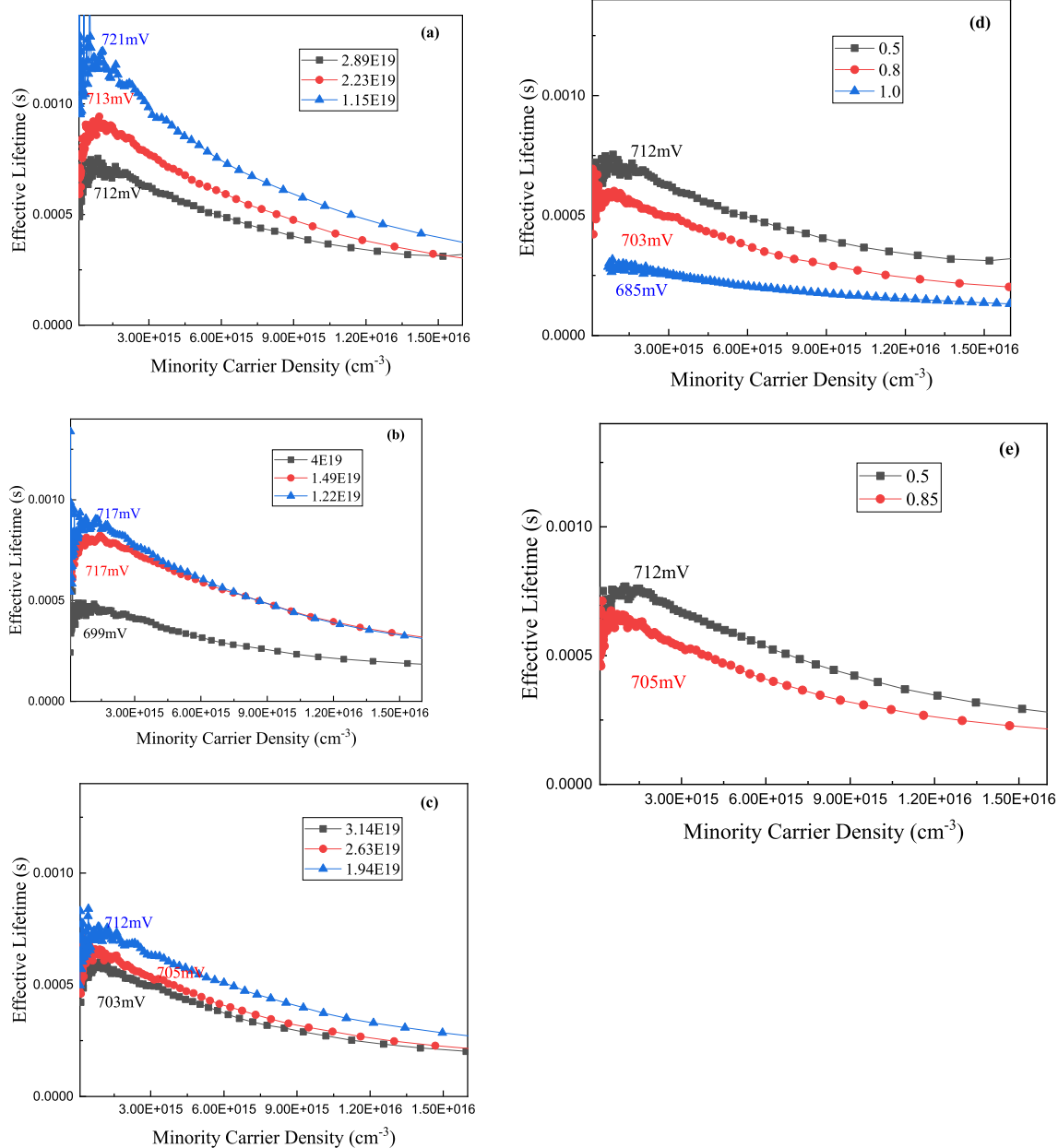


**Fig. 8.**  $iV_{oc}$  and Lifetime of the precursor structure wafers obtained from (a) emitter D1, (b) emitter D2, (c) emitter D3, (d) emitter N1 and (e) emitter N2.

**Table 3**Five group experiments of B-doped profiles and *I*-*V* parameters of TOPCon cells (Cell area of 251.99 cm<sup>2</sup>).

Processes	<i>N</i> <sub>max</sub> (atoms/cm <sup>3</sup> )	Junction depth (μm)	No.	<i>V</i> <sub>oc</sub> (V)	<i>J</i> <sub>sc</sub> (mA/cm <sup>2</sup> )	FF (%)	<i>R</i> <sub>ser</sub> (mohm.cm <sup>2</sup> )	<i>E</i> <sub>ff</sub> (%)	
D1	1.15E + 19	0.5	Median	5	0.694	41.12	80.02	4.11	22.85
	2.23E + 19		Ave		0.694	41.1	80.06	4.09	22.84
			Median	5	0.695	41.06	80.36	4.2	22.92
	2.89E + 19		Ave		0.695	41.05	80.36	4.17	22.91
			Median	4	0.692	40.99	80.71	3.89	22.89
			Ave		0.691	41	80.66	3.85	22.87
	1.22E + 19		Median	4	0.702	41.2	80.23	4.33	23.21
	1.49E + 19		Ave		0.702	41.22	80.24	4.31	23.21
D2	4.00E + 19	0.63	Median	5	0.701	41.09	80.91	3.94	23.32
			Ave		0.702	41.1	80.8	3.95	23.3
			Median	5	0.695	40.64	81.48	4.07	23
			Ave		0.694	40.63	81.42	4.07	22.97
D3	1.94E + 19	0.8	Median	5	0.702	41.01	81.09	4	23.34
			Ave		0.702	41	81.07	4.05	23.33
	2.63E + 19		Median	4	0.697	40.68	81.02	4.07	22.97
	3.14E + 19		Ave		0.697	40.66	81.04	4.07	22.98
			Median	5	0.696	40.54	81.24	3.91	22.91
N1	3.00E + 19	0.5	Ave		0.696	40.52	81.29	3.94	22.91
			Median	4	0.692	40.99	80.71	3.89	22.89
			Ave		0.691	41	80.66	3.85	22.87
			Median	5	0.697	40.64	81.05	4.27	22.96
			Ave		0.697	40.64	81.08	4.21	22.95
			Median	4	0.696	40.43	81.68	3.74	23
N2	2.60E + 19	0.5	Ave		0.697	40.43	81.68	3.74	23.01
			Median	4	0.697	41.16	80.29	4.21	23.02
			Ave		0.697	41.16	80.27	4.2	23.02
			Median	4	0.697	40.68	81.02	4.07	22.97
			Ave		0.697	40.66	81.05	4.07	22.98

Note: *N*<sub>max</sub>: the peak concentration; *V*<sub>oc</sub>: open circuit voltage; *J*<sub>sc</sub>: short circuit current density; *R*<sub>ser</sub>: series resistance; FF: fill factor; *E*<sub>ff</sub>: efficiency

the shallow D1 emitter sample with the peak concentration of  $1.15 \times 10^{19}$  atoms/cm<sup>3</sup> with a higher  $iV_{oc} = 721$  mV. A decrease of  $<10$  mV in *V*<sub>oc</sub> was observed at the deep p<sup>+</sup>-diffused region with 0.8 μm, while for the shallow p<sup>+</sup>-diffused region with 0.5 μm, the drop exceeds 15 mV on emitter N1 and N2. It was indicated that the profile depth of B-doped can minimize the *V*<sub>oc</sub> losses by effectively shielding the metal contacts from the minority charge carriers. Therefore, the junction depth is important as its calculation considers the effects of metal spikes penetrating the B-doped emitters (Wöhrle et al., 2016). To derive a high *J*<sub>sc</sub> and FF, a trade-off between the peak concentration and junction depth of the doping profile, which considers the effects of  $\rho_c$  and *J*<sub>0e</sub>, is inevitable (Schmidt et al., 2018). According to Fig. 9a, the ideal efficiency would be more than 23.4%, which would be possible if the peak concentration and junction depth of B-doped profile were  $1\text{--}1.5 \times 10^{19}$  atoms/cm<sup>3</sup> and 0.75–1.0 μm, respectively. In Fig. 9b, the junction depth has a stronger influence on the *V*<sub>oc</sub> than the peak concentration. To obtain a high *V*<sub>oc</sub>, a low peak concentration and deep junction of doping profiles are required due to the need to meet the conditions of corroded depth of the Ag/Al paste. To ascertain further the accuracy of the tested results, the total recombination activity in the cell (*J*<sub>0e,total</sub>) was calculated by using the measured values of *J*<sub>0e,passivated</sub> and *J*<sub>0e,metal</sub> according to equation (1). The saturation current density of the bulk (*J*<sub>0,bulk</sub>) was estimated from testing, about 8 fA/cm<sup>2</sup>. The cell *V*<sub>oc</sub> was calculated from *J*<sub>0e,total</sub> using an ideal one-diode model and compared against the measured *V*<sub>oc</sub>. A detailed calculation of the total *J*<sub>0e,total</sub> and comparison of the calculated and measured *V*<sub>oc</sub> values are shown in Table 4. The results show that there is a close match between the calculated *V*<sub>oc</sub> and the cell's measured *V*<sub>oc</sub>, except the peak concentration of  $2.89 \times 10^{19}$  atoms/cm<sup>3</sup> at  $d_1 = 0.5$

μm.

$$J_{0e,total} = \{(J_{0e,metal} \times f_f) + (J_{0e,passivated} \times (1 - f_f))\}(front) + \{(J_{0e,metal} \\ \times fr) + (J_{0e,passivated} \times (1 - fr))\}(rear) + J_{0,bulk} \quad (1)$$

Fig. 9c illustrates a negative correlation between *J*<sub>sc</sub> and the peak concentration/junction depth. To obtain a higher *J*<sub>sc</sub>, a lower peak concentration and shallow junction of doping profiles are required because of the improved short wavelength response of the internal quantum efficiency (IQE). However, FF is positively correlated with the peak concentration and junction depth (Fig. 9d), and the change in FF is mainly influenced by *R*<sub>ser</sub> (Fig. 9e). To obtain a high FF or a low *R*<sub>ser</sub>, a high peak concentration and deep junction are required.

### 3.6. Failure analysis

A current loss was used to be discussed in order to understand the effects of the B-doped profile. The simulated optical reflectance was in agreement with the results of the experimental reflection without any adjustments (Fig. 10); we did not find any significant optical reflection for those samples. The primary difference of IQE for emitters D1–D3 (Fig. 10a–c) and N1–N2 (Fig. 10d–e) occurred at short wavelengths  $< 550$  nm; their blue responses were significantly degraded by the higher peak concentration and deep junction of the B-doped profile. Especially, the IQE for emitter N2 with 1.0 μm exhibited a poor response at wavelengths  $< 1,000$  nm. These curves show that the values of *J*<sub>sc</sub> are decreased by increasing the peak concentration and junction depth of the B-doped profile, owing to the high recombination on the front surface (Fig. 9c&e).

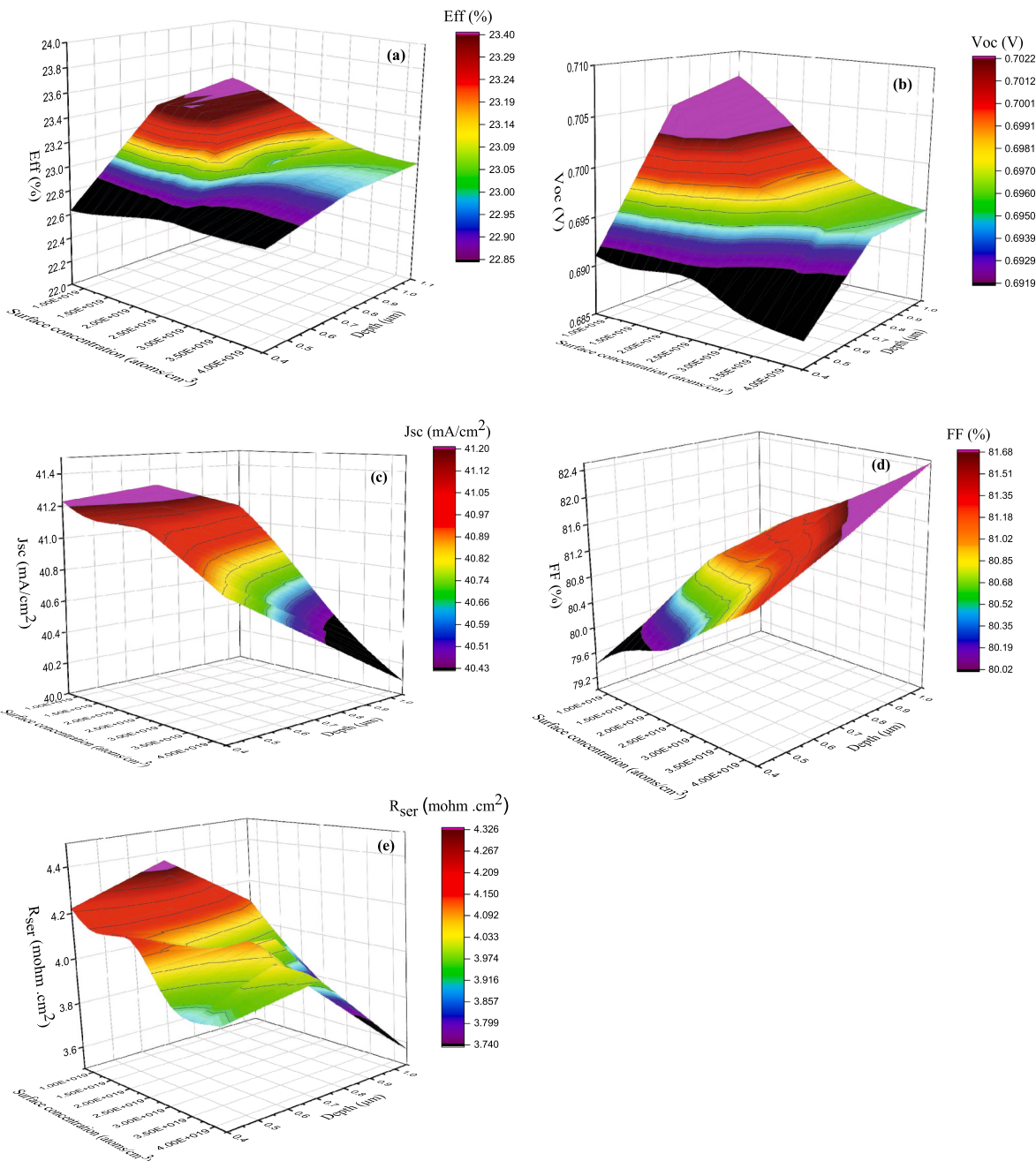


**Fig. 9.** (a)  $E_{\text{ff}}$ , (b)  $V_{\text{oc}}$ , (c)  $J_{\text{sc}}$ , (d) FF and (e)  $R_{\text{ser}}$  as a function of the junction depth and the peak concentration of B-doped profile.

**Table 4**Detailed calculation of  $V_{oc}$  using an ideal one-diode model from the measured values of  $J_{0e,passivated}$  and  $J_{0e,metal}$ .

Processes	D1			D2			D3			N1			N2	
$N_{max}$ (atoms/cm <sup>3</sup> )	1.15E + 19	2.23E + 19	2.89E + 19	1.22E + 19	1.49E + 19	4.00E + 19	1.94E + 19	2.63E + 19	3.14E + 19	3.00E + 19			2.60E + 19	
Junction depth (μm)	0.5			0.63			0.8			0.5	0.8	1	0.5	0.85
$J_{0e,metal}$ (front fingers) [fA/cm <sup>2</sup> ]	828	680	645	784	826.4	342.4	550	445.4	412	645	412	699.3	660.9	445.4
$J_{0e, passivated}$ (front) [fA/cm <sup>2</sup> ]	18.4	21.1	22.3	15.7	20.4	44.4	23.3	36.4	39.9	22.3	39.9	42.8	22.4	36.4
Metallized fraction (front fingers) ( $f_f$ ) [%]	1.50%													
$J_{0e,metal}$ (rear fingers) [fA/cm <sup>2</sup> ]	100													
$J_{0e, passivated}$ (rear) [fA/cm <sup>2</sup> ]	5													
Metallized fraction (rear fingers) ( $f_r$ ) [%]	2%													
$J_{0, bulk}$ [fA/cm <sup>2</sup> ]	8													
$J_{0e, total}$ [fA/cm <sup>2</sup> ]	45.4	45.9	46.5	42.1	47.4	63.8	46.1	57.4	60.4	46.5	60.4	67.5	46.9	57.4
$V_{oc}$ (calculated) [mV]	698	700	700	701	699	695	701	697	696	700	696	692	700	697
$V_{oc}$ (measured, average) [mV]	694	695	692	702	701	695	702	697	696	692	697	696	697	697

The loss of current density was analyzed via simulation (Fig. 11). Based on the Yablonovitch limit of 46.43 mA/cm<sup>2</sup>, the light-trapping ability of the solar cell may be estimated (Yablonovitch, 1987). From emitters D1–D3 (Fig. 11a–c) and N1–N2 (Fig. 11d–e), there were three main losses: one was the “blue loss” and the other “base collection loss.” Both losses lead to low short-circuit values. In this study, the recombination-induced current loss was due to the finite diffusion length in the emitter and in the wafer, which was mainly the higher peak concentration and deep junction of the B-doped profile. Especially, the deep junction 1.0 μm has a larger “blue loss” about 0.6 mA/cm<sup>2</sup> than others 0.3–0.4 mA/cm<sup>2</sup> and a larger “base collection loss” about 0.53 mA/cm<sup>2</sup> than others < 0.35 mA/cm<sup>2</sup>. This is consistent with the above QE results.

The last type of loss was the “non-uniformity loss,” which mainly originates from the difference in current density between a high-quality spot on the wafer and the average of the wafer. In this study, the main reason for this loss was that the uniformity of front passivation on the lower peak concentration and shallow junction were difficult to be controlled. For emitters D2, D3 and N1, besides these three losses, an additional loss exists, called “NIR parasitic absorb,” which occurs due to unremoved the wraparound of rear B layer with a higher peak concentration on the deep junction in the same rear-etching condition. Therefore, a good rear planarization could reduce the NIR parasitic absorb loss and improve the efficiency of the solar cells. We must consider all these factors to optimize the front side passivation.

The optimization of the B-doped process and front passivation could improve the efficiency and optical properties of the solar cells. Meanwhile, B-selective emitters with few emitter recombination, low contact resistance, and good blue response must be further optimized in order to increase the efficiency of the n-TOPCon solar cells.

#### 4. Conclusions

The emitter dark saturation current density under the passivation layer ( $J_{0e, passivated}$ ), the metallization-induced recombination current density under the metal contact ( $J_{0e, metal}$ ), and the  $I$ – $V$  parameters of the solar cell ( $J_{sc}$ ,  $V_{oc}$ , FF and  $E_{ff}$ ) were investigated as functions of the peak concentration and junction depth of B-doped profile. The best solar cell with a high  $E_{ff}$  (23.34%),  $V_{oc}$  (702 mV), and  $J_{sc}$  (41.01 mA/cm<sup>2</sup>) was obtained using the B-doped profile with junction depth of 0.8 μm and the peak concentration of  $1.94 \times 10^{19}$  atoms/cm<sup>3</sup>. The junction depth has a stronger influence on the  $V_{oc}$  than the peak concentration. A low peak concentration and deep junction of B-doped profiles are required for getting a high  $V_{oc}$ . The  $J_{sc}$  and the peak concentration/junction depth of

B-doped profile are negatively correlated. Both a low peak concentration and shallow junction of B-doped profiles are required for getting a high  $J_{sc}$ , which can improve the blue response of the IQE. However, we observed a positive linear relation between FF and the peak concentration/depth junction; the change in FF was mainly influenced by  $R_{ser}$ .

The results revealed that there was a significant negative correlation between the contact resistance ( $\rho_c$ ),  $iV_{oc}$ ,  $J_{sc}$  and the peak concentration, depth junction. However, the passivated emitter recombination ( $J_{0e, passivated}$ ) was positively correlated with the peak concentration and depth junction. The peak concentration was the most sensitive parameter with respect to the metallization-induced recombination ( $J_{0e, metal}$ ) in shallow emitters D1 and D2 compared with deep emitter D3, owing to a corroded depth of approximately 0.45–0.63 μm. The primary difference in the IQE for emitters D1–D3 and N1–N2 occurred at short wavelengths < 550 nm. The primary difference of IQE for the deep emitter (1.0 μm) had a poor bulk response at wavelengths < 1,000 nm. Subsequently, the emitter doping profiles satisfy the conditions of corroded depth and  $\rho_c$  of the Ag/Al paste, a balance between the peak concentration and junction depth must be found for obtaining a good  $V_{oc}$  and FF.

The optimization of B-diffusion processes (the peak concentration of  $1.15 \times 10^{19}$  atoms/cm<sup>3</sup>, junction depth of 0.75–1.0 μm) and front passivation could improve the efficiency and optical properties of the solar cells. Meanwhile, B-selective emitters with low emitter recombination, low contact resistance, and good blue response must be further optimized to increase the efficiency.

After the optimization of B-selective emitters and passivation processes, we manufactured industrial-grade TOPCon cells with efficiency ( $E_{ff}$ ),  $V_{oc}$ ,  $J_{sc}$ , and FF values as high as 23.7%, 709 mV, 40.8 mA/cm<sup>2</sup>, and 82% respectively.

#### CRediT authorship contribution statement

**Qinqin Wang:** Data curation, Formal analysis, Investigation, Methodology, Resources, Software, Writing – original draft, Writing – review & editing. **Wangping Wu:** Writing – review & editing. **Yunpeng Li:** Writing – review & editing. **Ling Yuan:** Resources. **Sanchuan Yang:** Resources. **Yufeng Sun:** Resources. **Songbo Yang:** Resources. **Qiang Zhang:** Resources. **Yujia Cao:** Resources. **Hui Qu:** Resources. **Ningyi Yuan:** Writing – review & editing, Supervision. **Jianning Ding:** Writing – review & editing.

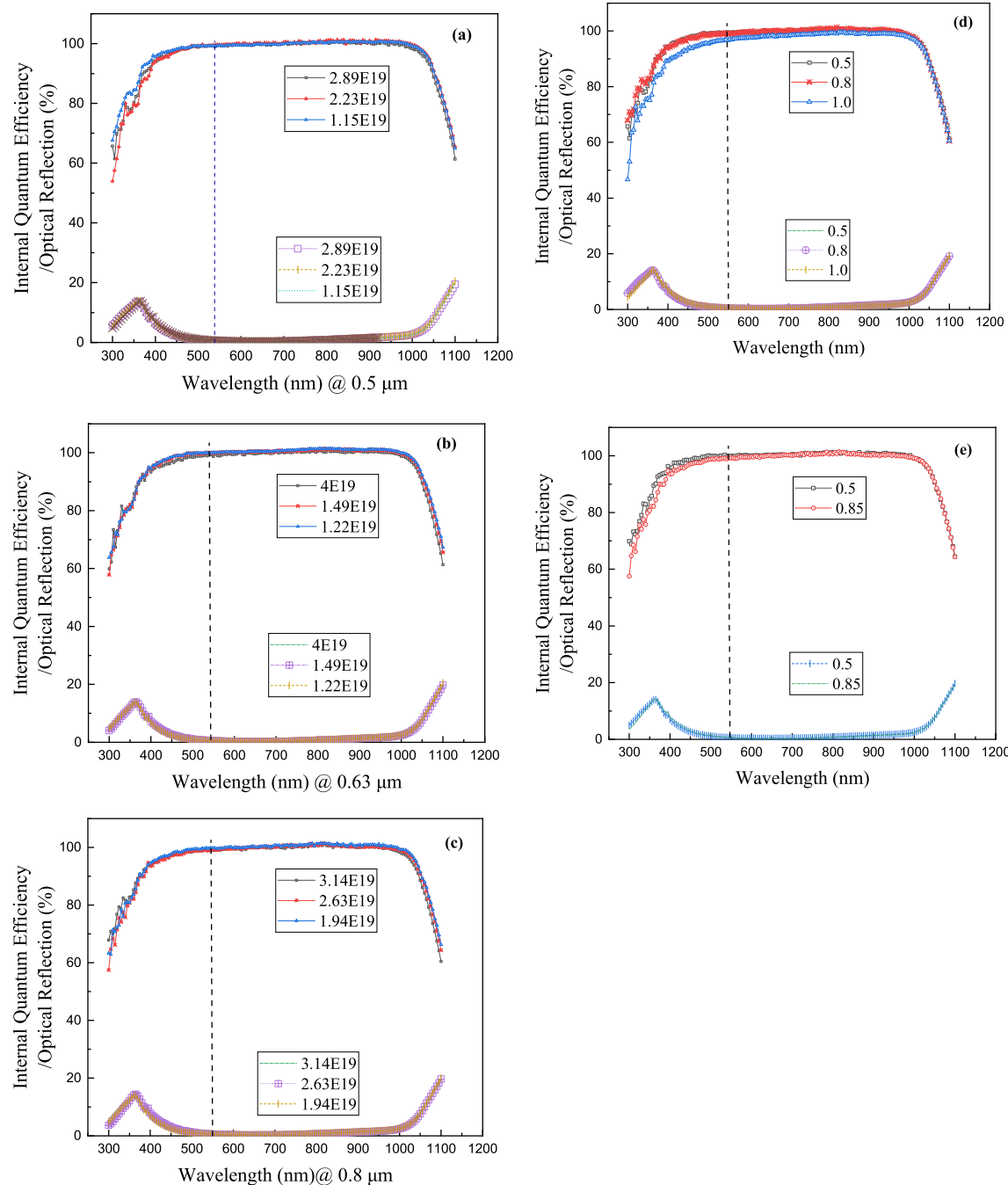


**Fig. 10.** The curve for internal quantum efficiency (IQE) and the dashed line curve for optical reflection for (a) emitter D1, (b) emitter D2, (c) emitter D3, (d) emitter N1 and (e) emitter N2.

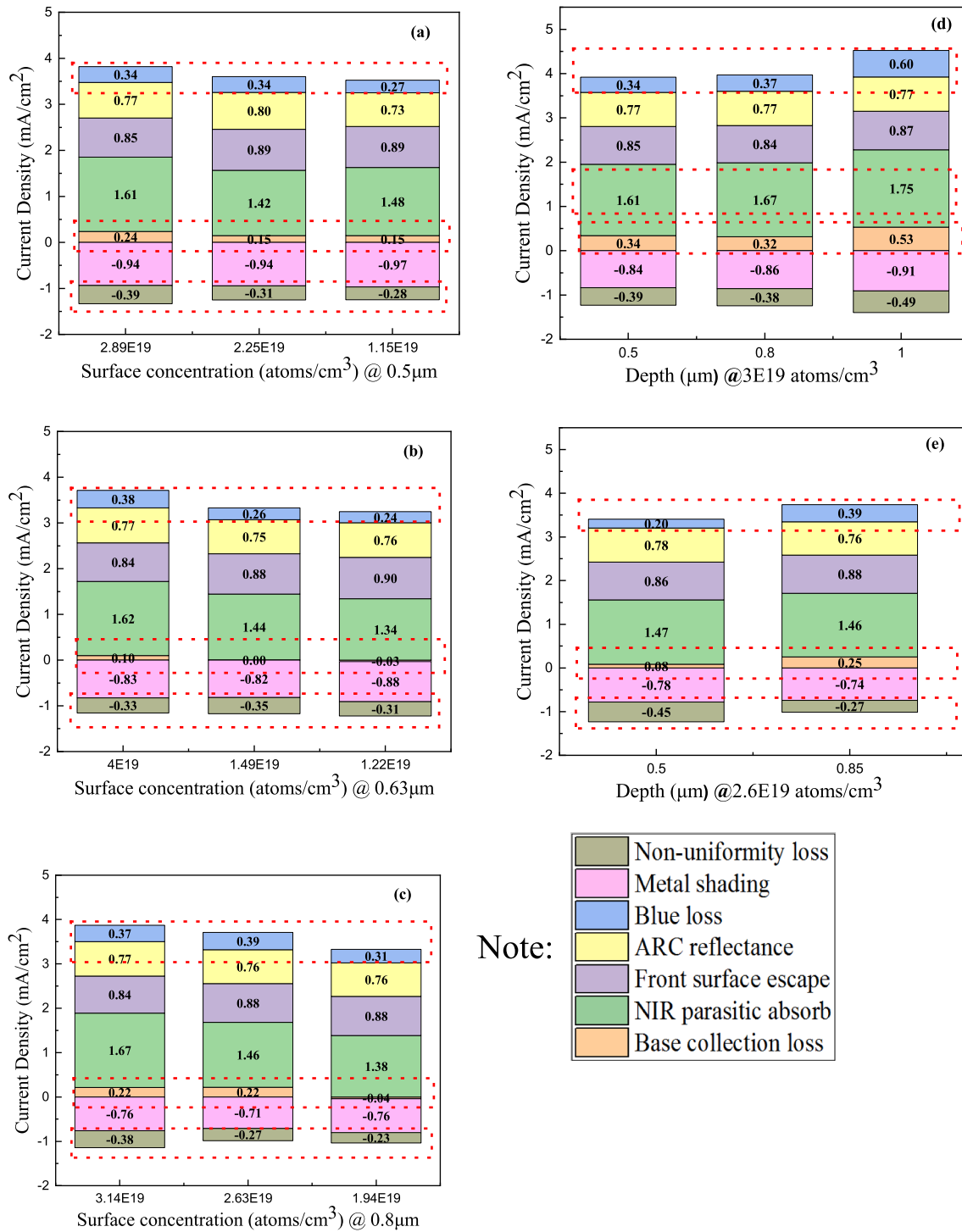


Fig. 11. Current loss mechanisms for (a) emitter D1, (b) emitter D2, (c) emitter D3, (d) emitter N1 and (e) emitter N2.

## Declaration of Competing Interest

The authors declare that they have no known competing financial interests or personal relationships that could have appeared to influence the work reported in this paper.

## Acknowledgements

This work has been partially supported by the National Key Research and Development Program of China (2018YFB1500300) and the Natural Science Foundation of Jiangsu Province (Grants No. BE2017006)

## Appendix A. Supplementary material

Supplementary data to this article can be found online at <https://doi.org/10.1016/j.solener.2021.08.075>.

## References

- Upadhyaya, A.D., Madani, K., Upadhyaya, V., et al., 2020. Boron Selective Emitter Formation With Un-metallized  $J_{SC}$  of  $13\text{FA}/\text{cm}^2$  For Silicon Solar Cell Applications. IEEE 47th Photovoltaic Specialists Conference (PVSC).
- Altermatt, P.P., Schumacher, J.O., Cuevas, A., Kerr, M.J., Glunz, S.W., King, R.R., Heiser, G., Schenk, A., 2002. Numerical modeling of highly doped Si: P emitters based on Fermi-Dirac statistics and self-consistent material parameters. *J. Appl. Phys.* 92 (6), 3187–3197.
- Armand, J., Oliver, C., Semmache, B., et al., 2011. Modeling and analysis of the emitter boron process under  $\text{BCl}_3$  and  $\text{O}_2$  for industrial silicon cells applications. 26th European Photovoltaic Solar Energy Conference and Exhibition.
- Benick, J., Hoex, B., van de Sanden, M.C.M., Kessels, W.M.M., Schultz, O., Glunz, S.W., 2008. High efficiency n-type Si solar cells on Al2O3-passivated boron emitters. *Appl. Phys. Lett.* 92 (25), 253504. <https://doi.org/10.1063/1.2945287>.
- Bock, R., Altermatt, P.P., Schmidt, J., 2008. Accurate extraction of doping profiles from electrochemical capacitance voltage measurements. In: Proceedings of the 23rd European Photovoltaic Solar Energy Conference and Exhibition, Valencia, Spain, pp. 1510–1513.
- Chen, D., Chen, Y., Wang, Z., et al., 2020. 24.58% total area efficiency of screen-printed, large area industrial silico solar cells with the tunnel oxide passivated contacts (i-TOPCon) design. *Sol. Energy Mater. Sol. Cells* 206, 110258.
- Chen, Y., Chen, D., Liu, C., et al., 2019. Mass production of industrial tunnel oxide passivated contacts (i-TOPCon) silicon solar cells with average efficiency over 23% and modules over 345 W. *Prog. Photovoltaics Res. Appl.* 27 (10), 827–834.
- Driean, M., Richter, A., Steinhauser, B., et al., 2020. Simultaneous Boron Emitter Diffusion and Crystallization of TOPCon Layers via Rapid Vapour-Phase Direct Doping. 37th European Photovoltaic Solar Energy Conference and Exhibition.
- Durán, J.C., Venier, G., Weht, R., 1991. Optimization of the junction depth and doping of solar cell emitters. *Solar Cells* 31 (6), 497–503.
- Duttagupta, S., Lin, F., Shetty, K.D., et al., 2012. State-of-the-art Surface Passivation of Boron Emitters using Inline PECVD AlOx/SiNx Stacks for Industrial High-Efficiency Silicon Wafer Solar Cells. Photovoltaic Specialists Conference.
- del Alamo, J.A., Swanson, R.M., 1984. The physics and modeling of heavily doped emitters. *Electron Devices IEEE Trans.* 31 (12), 1878–1888.
- Ebrahimi, P., Kolahdouz, M., Norouzi, M., Aghababa, H., Aletayeb, A., Asl-Soleimani, E., 2017. Selective boron diffusion without masking layer using boric acid for solar cell emitter formation. *J. Mater. Sci.: Mater. Electron.* 28 (15), 10794–10798.
- Edler, A., Mihailatchi, V.D., Kuduvilakathu, L.J., Comparotto, C., Kopecek, R., Harney, R., 2015. Metallization-induced recombination losses of bifacial silicon solar cells. *Prog. Photovoltaics Res. Appl.* 23 (5), 620–627.
- Feldmann, F., Bivour, M., Reichel, C., et al., 2013. A passivated rear contact for high efficiency n-type silicon solar cells enabling high VocS and FF>82%. In: in: 28th European PV Solar Energy Conference and Exhibition, pp. 988–992.
- Feldmann, F., Bivour, M., Reichel, C., et al., 2014. Passivated rear contacts for high efficiency n-type Si solar cells providing high-efficiency n-type Si solar cells providing high interface passivation quality and excellent transport characteristics. *Sol. Energy Mater. Sol. Cells* 120, 270–274.
- Fellmeth, T., Born, A., Kimmerle, A., Clement, F., Biro, D., Preu, R., 2011. Recombination at Metal-Emitter Interfaces of Front Contact Technologies for Highly Efficient Silicon Solar Cells. *Energy Procedia* 8, 115–121.
- Fritz, S., Konig, M., Riegel, S., Herguth, A., Hörteis, M., Hahn, G., 2015. Formation of Ag/Al screen-printing contacts on B emitters. *IEEE J. Photovoltaics* 5 (1), 145–151.
- Fritz, S., Engelhardt, J., Ebert, S., et al., 2016a. Contacting boron emitters on n-type silicon solar cells with aluminium-free silver screen-printing pastes. *Physica Status Solidi (RRL) - Rapid Research Lett.*, 10(4), 305–309.
- Fritz, S., Emre, E., Engelhardt, J., Ebert, S., Nowak, N., Booth, J., Hahn, G., 2016b. Contacting BBr 3-based boron emitters with aluminium-free screenprinting paste. *Energy Procedia* 92, 925–931.
- Fritz, S., Riegel, S., Gloger, S., Kohler, D., König, M., Hörtheis, M., Hahn, G., 2013. Influence of emitter properties on contact formation to p<sup>+</sup> silicon. *Energy Procedia* 38, 720–724.
- Grove, A.S., Leistikow, O., Sah, C.T., 1964. Redistribution of acceptor and donor impurities during thermal oxidation of silicon. *J. Appl. Phys.* 35 (9), 2695–2701.
- Haase, F., Hollemann, C., Schäfer, S., et al., 2018. Laser contact openings for local poly-Si-metal contacts enabling 26.1%-efficient POLO-IBC solar cells. *Solar Energy Mater. Solar Cells* 186, 184–193.
- Heinz, F.D., Breitwieser, M., Gundel, P., König, M., Hörteis, M., Warta, W., Schubert, M., 2014. Microscopic origin of the aluminium assisted spiking effects in n-type silicon solar cells. *Sol. Energy Mater. Sol. Cells* 131, 105–109.
- Hermle, M., Feldmann, F., Bivour, M., Goldschmidt, J.C., Glunz, S.W., 2020. Passivating contacts and tandem concepts: approaches for the highest silicon-based solar cell efficiencies. *Appl. Phys. Rev.* 7 (2), 021305. <https://doi.org/10.1063/1.5139202>.
- Huang, Y.-Y., Ok, Y.-W., Madani, K., Choi, W., Upadhyaya, A.D., Upadhyaya, V.D., Rohatgi, A., 2020. Fully screen-printed bifacial large area 22.6% N-type Si solar cell with lightly doped ion-implanted boron emitter and tunnel oxide passivated rear contact. *Sol. Energy Mater. Sol. Cells* 214, 110585. <https://doi.org/10.1016/j.solmat.2020.110585>.
- Kane, D., Swanson, R., 1985. Measurement of the emitter saturation current by a contactless photoconductivity decay method. *IEEE Photovoltaic Specialists Conf.* 18, 578–583.
- Kerp, H., Kim, S., Lago, R., et al., 2006. Development of screen printable contacts for P emitters in bifacial solar cells. In: in: Proceedings of the 21st European Photovoltaic Solar Energy Conference, pp. 892–894.
- Kiefer, F., Peibst, R., Ohrdes, T., et al., 2014. Emitter recombination current densities of boron emitters with silver/aluminum pastes. In: 40th IEEE Photovoltaic Specialists Conference (PVSC), pp. 2808–2812.
- Kiefer, F., Krugener, J., Heinemeyer, F., Osten, H.J., Brendel, R., Peibst, R., 2016. Structural investigation of printed Ag/Al contacts on silicon and numerical modeling of their contact recombination. *IEEE J. Photovoltaics* 6 (5), 1175–1182.
- Koduvilakathu, L.J., Mihailatchi, V.D., Olivet, S., Rudolph, D., Cabrera, E., Kopecek, R., 2015. Two-dimensional modeling of the metallization-induced recombination losses of screen-printed solar cells. *IEEE J. Photovoltaics* 5 (1), 159–165.
- Kopecek, R., Buck, T., Libal, J., et al., 2005. Large area n-type multicrystalline silicon solar cells with B-emitter: Efficiencies exceeding 14%. In: in: Proceedings of the 15th International Photovoltaic Science and Engineering Conference, pp. 892–893.
- Lago, R., Pérez, L., Kerp, H., Freire, I., Hoces, I., Azkona, N., Recart, F., Jimeno, J.C., 2010. Screen printing metallization of boron emitters. *Prog. Photovoltaics Res. Appl.* 18 (1), 20–27.
- Li, M.J., Wong, J., Chen, N., et al., 2018. Determination of metallization induced recombination losses of screen printed solar cell contacts and its dependence on the doping profile. *IEEE J. Photovoltaics* 8 (99), 1–8.
- Li, M., Wong, J., Wang, E.-C., Rodriguez, J., Duttagupta, S., Samudra, G., Aberle, A.G., Stangl, R., 2019. Predictive simulation framework for boron diffused p<sup>+</sup> layer optimization: Sensitivity analysis of boron tube diffusion process parameters of industrial n-type silicon wafer solar cells. *Sol. Energy Mater. Sol. Cells* 189, 63–74.
- Lin, W., Chen, D., Liu, C., et al., 2020. Green-laser-doped selective emitters with separate BBr 3 diffusion processes for high-efficiency n-type silicon solar cells. *Sol. Energy Mater. Sol. Cells* 210, 110462. <https://doi.org/10.1016/j.solmat.2020.110462>.
- Liú, B., Chen, Y., Yang, Y., et al., 2016. Improved evaluation of saturation currents and bulk lifetime in industrial Si solar cells by the quasi steady state photo conductance decay method. *Sol. Energy Mater. Sol. Cells* 149, 258–265.
- Lohmüller, E., Fertig, F., Werner, S., Geismeyer, I., Clement, F., Biro, D., 2014a. Reverse bias behavior of diffused and screen-printed n-type Cz-Si solar cells. *IEEE J. Photovoltaics* 4 (6), 1483–1490.
- Lohmüller, E., Werner, S., Thaidigsmann, B., et al., 2014b. The HIP-MWT+ solar cell concept on n-type silicon and metallization-induced voltage losses. In: 29th European Photovoltaic Solar Energy Conference and Exhibition. pp. 635–641.
- Lohmüller, E., Werner, S., Hoenig, R., Greulich, J., Clement, F., 2015. Impact of boron doping profiles on the specific contact resistance of screen printed Ag-Al contacts on silicon. *Sol. Energy Mater. Sol. Cells* 142, 2–11.
- Lohmüller, E., Lohmüller (née Werner), S., Wöhrle, N., Belledin, U., Wolf, A., 2018. BBr 3 diffusion with second deposition for laser-doped selective emitters from borosilicate glass. *Sol. Energy Mater. Sol. Cells* 186, 291–299.
- Mihailatchi, V.D., Chu, H.F., Lossen, J., et al., 2018. Surface Passivation of Boron-Diffused Junctions by a Borosilicate Glass and In Situ Grown Silicon Dioxide Interface Layer. *IEEE J. Photovoltaics* 1–6.
- Monna, R., Sanzone, V., Diaz, J., Veschetto, Y., 2016. Influence of the BCl3 Diffusion Process Homogeneity on the Surface Passivation of n-type PERT Solar Cells. *Energy Procedia* 92, 479–485.
- Oliver, C., Semmache, B., Cuminal, Y., et al., 2010. Implementation of boron emitters using BCl3 diffusion process for industrial silicon solar cells fabrication. In: 25th European Photovoltaic Solar Energy Conference and Exhibition, pp. 1930–1933.
- Ok, Y.-W., Upadhyaya, V.D., Upadhyaya, A.D., et al., 2016. Screen printed, large area bifacial selective emitter N-PERT cells using single-step implantation through laser patterned dielectric layer. 43rd IEEE Photovoltaic Specialists Conference (PVSC).
- Padhamnath, P., Wong, J., Nagarajan, B., et al., 2019. Metal contact recombination in monoPoly™ solar cells with screen-printed & fire-through contacts. *Sol. Energy Mater. Sol. Cells* 192, 109–116.
- Pal, B., Ray, S., Gangopadhyay, U., Ray, P.P., 2019. Novel technique for fabrication of n-type crystalline silicon selective emitter for solar cell processing. *Mater. Res. Express* 6 (7), 075523. <https://doi.org/10.1088/2053-1591/ab18ee>.
- Peiner, E., Schlachetzki, A., Krüger, D., 1995. Doping profile analysis in Si by electrochemical capacitance–voltage measurements. *J. Electrochem. Soc.* 142 (2), 576–580.
- Polzin, J.I., Feldmann, F., Steinhauser, B., et al., 2018. Realization of TOPCon using industrial scale PECVD equipment. In: The 8th International Conference On Crystalline Silicon Photovoltaics. Lausanne, Switzerland.

- PV-magazine. 2020. Jinko claims 24.79% efficiency for n-type monocrystalline cell. [https://www.pv-magazine.com/2021/01/06/jinkosolar-claims-24-9-efficiency-for-n-typemonocrystalline-cell/#:text=2020-JinkoSolar%20claims%2024.9%25%20efficiency%20for%20n%20type%20monocrystalline%20cell,Solar%20Energy%20Research%20\(ISFH\).&text=Jinko%20has%20secured%20enough%20glass%20to%20produce%2059%20GW%20of%20modules](https://www.pv-magazine.com/2021/01/06/jinkosolar-claims-24-9-efficiency-for-n-typemonocrystalline-cell/#:text=2020-JinkoSolar%20claims%2024.9%25%20efficiency%20for%20n%20type%20monocrystalline%20cell,Solar%20Energy%20Research%20(ISFH).&text=Jinko%20has%20secured%20enough%20glass%20to%20produce%2059%20GW%20of%20modules).
- Richter, A., Benick, J., Feldmann, F., et al., 2018. Tunnel oxide passivating electron contacts as full-area rear emitter of high efficiency p-type silicon solar cells. *Prog. Photovolt.: Res. Appl.* 26, 579–586.
- Richter A., Muller R., Benick J., et al., 2020. 26% efficiency with both sides contacted silicon solar cells: front vs rear junction cell architecture. In: presented at the 10th International Conference on Crystalline Silicon Photovoltaics.
- Ryu, K., Madani, K., Rohatgi, A., Ok, Y.-W., 2017. High efficiency screen-printed n-type silicon solar cell using co-diffusion of APCVD boron emitter and  $\text{POCl}_3$  back surface field. *Curr. Appl. Phys.* 18 (2), 231–235.
- Schiele, Y., Joos, S., Hahn, G., Terheiden, B., 2014. Etch-back of  $\text{p}^+$  structures for selective boron emitters in n-type c-Si solar cells. *Energy Procedia* 55, 295–301.
- Schmidt, J., Peibst, R., Brendel, R., 2018. Surface passivation of crystalline silicon solar cells: Present and future. *Sol. Energy Mater. Sol. Cells* 187, 39–54.
- Schultz-Wittmann O., Turner, A., Eggleston, B., et al., 2016. High volume manufacturing of high efficiency crystalline silicon solar cells with shielded metal contacts. In: 32nd European Photovoltaic Solar Energy Conference and Exhibition, Munich, Germany, 22/6, pp. 456–459.
- Sinton R.A., Cuevas A., Stuckings M., 1996. Quasi-steady-state photoconductance, a new method for solar cell material and device characterization. In: Conference Record of the 25th IEEE Photovoltaic Specialists Conference, Washington DC, USA, 457–460.
- Tao, Y., Madani, K., Cho, E., et al., 2017. High-efficiency selective boron emitter formed by wet chemical etch-back for n-type screen-printed Si solar cells. *Appl. Phys. Lett.* 110.
- Tetzlaff, D., Krügener, J., Larionova, Y., Reiter, S., Turcu, M., Haase, F., Brendel, R., Peibst, R., Höhne, U., Kähler, J.-D., Wietler, T.F., 2017. A simple method for pinhole detection in carrier selective POLO-junctions for high efficiency silicon solar cells. *Sol. Energy Mater. Sol. Cells* 173, 106–110.
- Wang, Q., Wu, W., Yuan, N., Li, Y., Zhang, Y.i., Ding, J., 2020a. Influence of  $\text{SiO}_x$  film thickness on electrical performance and efficiency of TOPCon solar cells. *Sol. Energy Mater. Sol. Cells* 208, 110423. <https://doi.org/10.1016/j.solmat.2020.110423>.
- Wang, Q., Wu, W., Chen, D., Yuan, L., Yang, S., Sun, Y., yang, S., Zhang, Q., Cao, Y., Qu, H., Yuan, N., Ding, J., 2020b. Study on the cleaning process of n+-poly-Si wraparound removal of TOPCon solar cells. *Sol. Energy* 211, 324–335.
- Werner, S., Lohmüller, E., Wolf, A., Clement, F., 2016. Extending the limits of screen-printed metallization of phosphorus- and boron-doped surfaces. *Sol. Energy Mater. Sol. Cells* 158, 37–42.
- Wong, J., Raj, S., Ho, J.W., Wang, J., Lin, J., 2016. Voltage Loss Analysis for Bifacial Silicon Solar Cells: Case for Two-Dimensional Large-Area Modeling. *IEEE J. Photovoltaics* 6 (6), 1421–1426.
- Wöhrl, N., Lohmüller, E., Greulich, J., Werner, S., Mack, S., 2016. Towards understanding the characteristics of Ag-Al spiking on boron-doped silicon for solar cells. *Sol. Energy Mater. Sol. Cells* 146, 72–79.
- Yablonovitch, E., 1987. Statistical ray optics. *J. Optical Soc. Am.* 72 (7), 899–907.
- Yoon, W., Moore, J., Lochtefeld, A., Kotulak, N., Scheiman, D., Barnett, A., Jenkins, P., Walters, R., 2017. Advanced surface passivation of epitaxial boron emitters for high-efficiency ultrathin crystalline silicon solar cells. *Jpn. J. Appl. Phys.* 56 (8S2), 08MB11. <https://doi.org/10.7567/JJAP.56.08MB11>.
- Yu, B.o., Shi, J., Li, F., Wang, H., Pang, L., Liu, K., Zhang, D., Wu, C., Liu, Y., Chen, J., Lu, W., Cong, R., Yu, W., 2021. Selective tunnel oxide passivated contact on the emitter of large-size n-type TOPCon bifacial solar cells. *J. Alloy. Compd.* 870, 159679. <https://doi.org/10.1016/j.jallcom.2021.159679>.
- Zhou, Y., Tao, K., Liu, A.M., et al., 2020. Study of boron diffusion for  $\text{p}^+$  emitter of large area N-type TOPCon silicon solar cells. *Appl. Phys. A* 126 (9), 671.
- Zhu, P., Liu, Y., Cao, C., Tian, J., Zhang, A., Wang, D., 2021. Low Recombination Firing-Through Al Paste for N-Type Solar Cell with BoronEmitter. *Materials* 14 (4), 765. <https://doi.org/10.3390/ma14040765>.